nature portfolio

https://doi.org/10.1038/s41586-022-04568-6

Supplementary information

Programmable heating and quenching for efficient thermochemical synthesis

In the format provided by the authors and unedited

Supplementary Information for

Programmable Heating and Quenching for Efficient Thermochemical Synthesis

Qi Dong[1†], Yonggang Yao[1†], Sichao Cheng[2†], Konstantinos Alexopoulos[3†], Jinlong Gao[1], Sanjana Srinivas[3], Yifan Wang[3], Yong Pei[4], Chaolun Zheng[4], Alexandra H. Brozena[1], Hao Zhao[5], Xizheng Wang[1], Hilal Ezgi Toraman[3], Bao Yang[4], Ioannis G. Kevrekidis[6], Yiguang Ju[5], Dionisios G. Vlachos[3*], Dongxia Liu[2*], Liangbing Hu[1,7*]

[1]Department of Materials Science and Engineering, University of Maryland, College Park, Maryland 20742, United States

[2]Department of Chemical and Biomolecular Engineering, University of Maryland, College Park, Maryland 20742, United States

[3]Department of Chemical and Biomolecular Engineering, University of Delaware, Newark, Delaware 19716, United States

[4]Department of Mechanical Engineering, University of Maryland, College Park, Maryland 20742, United States

[5]Department of Mechanical and Aerospace Engineering, Princeton University, Princeton, New Jersey 08544, United States

[6]Department of Chemical and Biomolecular Engineering, Department of Applied Mathematics and Statistics, Johns Hopkins University, Baltimore, Maryland 21218, United States

[7]Center for Materials Innovation, University of Maryland, College Park, Maryland 20742, United States

[†]These authors contributed equally to this work.

[*]binghu@umd.edu; liud@umd.edu; vlachos@udel.edu

Table of Contents

Supplementary Methods

Materials and instruments

Carbon paper (Freudenburg H23 gas diffusion layer) and carbon felt (AvCarb G475A) were obtained from Fuel Cell Store. Carbon felt (ACF 1000) was obtained from Fuel Cell Earth. The ACF 1000 carbon felt was used to study the morphological evolution of the catalyst. The AvCarb G475A carbon felt was found to be more stable against the rapid temperature change by programmable heating and quenching (PHQ), while the ACF 1000 carbon felt may break during long-term PHQ operations. Ruthenium (Ru) chloride hydrate, iron (Fe) chloride, hydrochloric acid, sodium hydroxide, sodium citrate, sodium hypochlorite, salicylic acid, sodium nitroferricyanide, and ammonium chloride of at least reagent grade were purchased from Sigma Aldrich. The carbon felt was loaded with Ru (2 wt%) or Fe catalyst (2 wt%) using a method described in our previous work[42]. All carbon materials were rinsed with ethanol and acetone, followed by overnight vacuum drying prior to installation in the heating device. The carbon materials were additionally preheated in Ar atmosphere for 2 h before each test due to the high surface area to remove moisture. Mirror-like multipurpose 110 copper wire (99.9%, 0.04" diameter) and multipurpose 110 copper sheets (99.9%, 0.002" thickness) were obtained from McMaster Carr. The copper materials were cleaned by acetone and dried under vacuum prior to installation in the heating device. Alumina ceramic protection tubes (99.8%, 0.125" outer diameter and 0.062" inner diameter, maximum temperature 2,223 K) were obtained from Omega and used without further cleaning. A solid-state relay device with DC input and DC output (maximum current 25 A) was obtained from Omega. The input signal to the solid-state relay was provided by a sourcemeter (Keithley, Model 2425). The output signal was provided by a power source (Volteq, 75 V, 20 A).

Reactor setup

The dimensions of the carbon paper used for the CH_4 pyrolysis reaction were 40 mm × 8 mm in size, with 20 mm × 8 mm exposed during the PHQ operations, with the remaining distance at each end being wrapped with copper foil. The dimensions of the carbon felt used in the NH_3 synthesis were 35 mm × 8 mm in size, with 15 mm × 8 mm exposed during the PHQ operations, with the remaining distance at each end being wrapped with copper foil. The lengths of the carbon paper shown in the digital images (but not for testing the reaction products) were increased for better demonstration. The wrapped region was further connected with copper wire to secure the electrical connection. No additional conductive glue or paste was needed to improve the electrical contact. The copper wire was then inserted through the alumina ceramic protection tube and connected with the power supply. Each end of the alumina ceramic protection tube was sealed with epoxy (Gorilla) ($T < 373$ K). The carbon heating element, copper material, and alumina ceramic protection tubes were placed in a quartz tube reactor (1/2"), which was connected with Swagelok Ultra-Torr tee fittings on each end. One port of the tee fitting was used for the electrical connection while the other was used for the gas inlet or outlet. A thermocouple was attached to the quartz tube close to the carbon material to monitor the temperature of the quartz tube during PHQ operations. The measured temperature was used to establish boundary conditions in the modeling efforts. Continuous heating for CH_4 pyrolysis was conducted using a tube furnace. Continuous heating for NH_3 synthesis was conducted using the catalyst-loaded or bare carbon felt as the Joule-heating element.

Product detection for CH_4 pyrolysis

The outlet product stream from the reactor was connected to and examined by gas chromatography (GC, Agilent 6890N) equipped with a DB-Wax column connected to a flame ionization detector as well as a ShinCarbon ST packed column connected to a thermal conductivity detector. A mixture of Ar and CH_4 was fed into the reactor, where Ar was used as an internal standard and balance gas. The percent conversion of CH_4 (X_{CH4}) was calculated according to Equation 1, where $A_{i,in}$ (i = CH_4 or Ar), which is the integrated peak area from the GC analysis, was determined from at least two initial GC calibration injections before the PHQ operation for each run.

$$X_{CH_4} = \frac{\left(\frac{A_{CH_{4,in}}}{A_{Ar,in}}\right) - \left(\frac{A_{CH_{4,out}}}{A_{Ar,out}}\right)}{\left(\frac{A_{CH_{4,in}}}{A_{Ar,in}}\right)} \quad 1$$

After the installation, the reactor was purged with 30 standard cubic centimeters per minute (sccm) Ar for 1 h, followed by feeding a mixed stream of CH_4 and Ar into the reactor for another 1 h until reaching a steady-state. Each data point was collected after running the reaction for ~26 mins. Product formation rates ($\dot{n}_{product}$) were calculated from the response factor according to Equation 2, where RF represents the response factor of each product with respect to Ar from the GC analysis, A is the integrated peak area from the GC analysis, and $i \geq 1$ (including CH_4).

$$\dot{n}_{C_iH_j}[mmol/min] = \frac{A_{C_iH_j}}{A_{Ar}} \times \dot{n}_{Ar,in} \times RF_{C_iH_j/Ar} \quad 2$$

The coke formation rate ($\dot{n}_{coke}$) was calculated according to Equation 3 based on the initial CH_4 feed flow rate, where $i \geq 1$ (including $\dot{n}_{CH_4,out}$).

$$\dot{n}_{coke}[mmol/min] = \dot{n}_{CH_4,in} - \sum(\dot{n}_{C_iH_j} \times i) \quad 3$$

The selectivity of CH_4 to each gaseous product (S) was calculated according to Equation 4, where $i \geq 2$ (not including CH_4).

$$S_{product}[mol\ \%] = \left(\frac{\dot{n}_{C_iH_j} \times i}{\sum\left(\dot{n}_{C_iH_j} \times i\right) + \dot{n}_{coke}}\right) \quad 4$$

The selectivity of CH_4 to coke products (S_{coke}) was calculated according to Equation 5, where $i \geq 2$ (not including CH_4). Note the unaccounted species $\dot{n}_{coke}$ include actual coke and other products with large molecular weights, which we considered to be coke-like species.

$$S_{coke}[mol\ \%] = \left(\frac{\dot{n}_{coke}}{\sum\left(\dot{n}_{C_iH_j} \times i\right) + \dot{n}_{coke}}\right) \quad 5$$

All reactions were conducted under ambient pressure (1 atm). The inlet gas temperature was 298 K in all cases. A flow rate of 24 sccm (90 mol% CH_4, 10 mol% Ar) was used for comparing continuous heating and PHQ methods (Fig. 3a). A flow rate of 4 sccm (75 mol% CH_4, 25 mol% Ar) was used for detailed studies on T_{high} and the pulse duration (Fig. 3b–d, with one data point from Fig. 3c being used in Fig. 1c for comparing PHQ and continuous heating, due to their comparable conversions). With a lower flow rate of 4 sccm, the conversion was relatively high so that the influences by T_{high} and the pulse duration could be better unveiled.

Note that the temperature of the electric circuit components (*e.g.*, Cu wires) remained lower than $T_{avg.}$ during PHQ operations due to their low electrical resistivity (therefore low heat generation during Joule heating), large heat capacity, and high thermal conductivity. A control experiment showed ~0% CH_4 conversion in the presence of the electric circuit components (*e.g.*, Cu wires) under continuous heating by a furnace at 900 K (> $T_{avg.}$), ruling out potential artifacts in the PHQ process.

Product detection for NH_3 synthesis

A flow rate of 20 sccm (75 mol% N_2, 25 mol% H_2) was used for NH_3 synthesis. All reactions were conducted under ambient pressure (1 atm). While industrial NH_3 synthesis is normally conducted at high pressures, in order to simplify our reactor design, we used ambient conditions to compare the NH_3 synthesis rates by PHQ and continuous heating, both using carbon felt as the heating element. Note that the presence of an active catalyst (*e.g.*, Ru or Fe) is critical, without which the NH_3 synthesis rate is close to zero by either PHQ or continuous heating using the tested conditions (not shown in the figures), which also suggests that the carbon felt and the electric circuit components (*e.g.*, Cu wire) are catalytically inactive in these processes.

NH_3 was detected using the Berthelot method (*i.e.*, the indophenol blue method, ref. [40]). In a typical process, 0.05 M hydrochloric acid solution was used to collect the NH_3 synthesized by PHQ and continuous heating. The reactant and product mixture passed through a gas bubbler into the hydrochloric acid solution at the downstream of the reactor. At each sampling point, 0.5 mL of the collected solution was used for quantification by UV-Vis spectrometry. The characteristic color was developed after the addition of three solutions in sequence: A) 1 M sodium hydroxide with 5 wt% sodium citrate and 5 wt% salicylic acid; B) 0.05 M sodium hypochlorite; and C) 1 wt% sodium nitroferricyanide. These solutions were added with a volume ratio of 1:0.5:0.1 (*e.g.*, 0.5 mL, 0.25 mL, and 0.05 mL, for a NH_3 containing solution of 0.5 mL). After mixing and storing in the dark for 2 h, the resulting solution was measured using a UV-Vis spectrometer (PerkinElmer). The adsorption intensity at 655 nm was chosen to represent the concentration of the formed indophenol blue. The adsorption intensity was calibrated to the NH_3 concentration using ammonium chloride with concentrations from 0 to 10 μg/mL. For NH_3-containing solution with a concentration higher than 10 μg/mL, the solution was diluted and then measured using the above procedure.

Programming electrical signal

A high accuracy sourcemeter (Keithley, Model 2425) was used to program the electrical signal for PHQ operations. Depending on the length of the high-temperature pulse desired, for each heating cycle the initial time duration was set as "power on" (*e.g.*, 0.02 s on) while the remaining time up to 1.1 s was set as "power off" (*e.g.*, 1.08 s off). Due to the gradual change of the defect level and crystallinity of the carbon heater during PHQ operations, which results in the gradual change of its resistance, the power input may need to be adjusted to maintain the desired peak temperature.

Temperature acquisition

The temperature evolution of the carbon-based heating element was measured using a Vision Research Phantom Miro M110 high-speed camera based on color ratio pyrometry, with videos recorded at 1000 frames/s. The temperature was calculated by applying the gray-body assumption

substituted in Planck's Law and integrating over the entire spectrum where the camera is sensitive (*i.e.*, 400–1,100 nm; shown in Equation 6)[43].

$$\frac{I_i}{I_j} = \frac{\psi_i \int L(\varepsilon, \lambda, T)\chi_i(\lambda)d\lambda}{\psi_j \int L(\varepsilon, \lambda, T)\chi_j(\lambda)d\lambda} \quad 6$$

in which I_i is the intensity of a color channel (*i.e.*, red, green or blue), ψ_i is the channel gain, ε is the emissivity, and χ_i is the spectral response. Calibration was achieved by a Newport Oriel 67000 Series Blackbody Infrared Light Source and calibration factors C_{gr} (green/red), C_{bg} (blue/green), and C_{br} (blue/red) can be obtained by comparing the measured values to the theoretical ones, as shown in Equation 7[43].

$$\left(\frac{I_i}{I_j}\right) = C_{ij}\left(\frac{I_i}{I_j}\right)_{\emptyset} \quad 7$$

At each pixel, to recover values for the red, green, and blue channels, the demosaicing routine in MATLAB was used with the camera's Bayer color filter array. Temperature estimates were made using color ratio pyrometry in which three color channels (red, green, and blue) were calculated and then matched to a gray-body calibration curve. The error in the reported temperature values is nominally ~100 K. For the temperature profile, only unsaturated pixels above the black level and within the error threshold were included to report the mean and median temperature of the frame for a contiguous area of at least 10 acceptable pixels. The temperature of the carbon heater was calculated by fitting the emitted light spectra according to the gray body radiation and the following equation:

$$B_\lambda(\lambda, T) = \gamma\varepsilon_{gray}\frac{2hc^2}{\lambda^5}\frac{1}{e^{hc/\lambda k_B T} - 1} \quad 8$$

in which k_B is the Boltzmann constant, λ is the wavelength, h is Planck's constant, c is the speed of light, and ε_{gray} is the gray body emissivity. Scaling constant γ and temperature T are the fitting parameters for this equation.

As the color ratio pyrometry method has a lower detection limit of ~1,100 K, only a part of the temperature profile can be accurately captured. Therefore, we used a linear temperature ramp followed by exponential decay of temperature based on the measured T_{high}, initial cooling rate, and T_{low} (measured by a thermocouple) to estimate the temperature profiles shown in Fig. 1b and Fig. 4b, which schematically demonstrate the fast heating and cooling processes by the PHQ technique.

Spectroscopic and microscopic characterization

X-ray diffraction (XRD) was conducted using a PANalytical X'Pert Pro diffractometer with Cu Kα radiation. Raman spectra were obtained with a micro-Raman system (XploRA, Horiba) equipped with a 532 nm laser. Scanning electron microscopy (SEM) images were taken using a JEOL 6340F microscope operated at a 10 kV accelerating voltage.

Modeling of the temperature profile of the gas molecules

The temperature distribution was simulated using a 3D transient numerical model. The model was constructed by a commercial software called ANSYS Fluent. The model takes into consideration the means of heat transfer by conduction, convection, and radiation. The reaction heat required for CH_4 pyrolysis was also included, which was found to be insignificant compared to other types of heat transfer. Geometrical parameters used for the model are listed in Supplementary Table 2 unless otherwise noted. The temperature at the wall of the quartz tube was set as 600 K based on

the experimental measurements by a thermocouple. The inlet gas temperature and initial temperature were also assumed to be 600 K (trough temperature, T_{low} = 600 K). The flow rate of the inlet gas mixture was set as 4 sccm with a molar ratio of CH_4:Ar equal to 3:1, same as the experimental conditions. A time-dependent temperature ramp based on experimental measurements was applied to the carbon paper every 1.1 s to simulate the PHQ operation. The total simulation time was 3.3 s, during which the temperature profile of the gas molecules started to repeat itself in every period starting from 2.2 s. Therefore, the period of 2.2 to 3.3 s was selected to plot as the "first" period (0 to 1.1 s) in Fig. 2g.

The material properties used in this numerical model are listed in Supplementary Table 3 unless otherwise noted (ref. [19])[44-54]. The density of the carbon paper was provided by the vendor. The specific heat capacity and optical properties of the carbon paper were assumed to be the same as those of graphite (ref. [19]). The maximum heat capacity of the carbon paper (0.033 J/K) is the product of the specific heat capacity of graphite at 2,400 K and the mass of the carbon paper. The carbon paper exhibits anisotropic thermal conductivity due to its layered structured. Based on related studies[44-47], the thermal conductivity was assumed to be 10 W/m•K and 0.2 W/m•K with respect to the direction parallel to the layer and to the direction perpendicular to the layer, respectively. The optical properties, density, and thermal conductivity of the carbon paper were assumed to be temperature-independent in the numerical model.

The specific heat of the gas mixture $c_{p,mix}$ was calculated by:

$$c_{p,\mathrm{mix}} = \sum_{i=1}^{n} x_i c_{p,i} \tag{9}$$

where x_i and $c_{p,i}$ are the molar fraction and the molar specific heat of the i^{th} component, respectively.

The thermal conductivity of the gas mixture λ_{mix} was calculated using Wilke's mixing rule[55]:

$$\lambda_{\mathrm{mix}} = \sum_{i=1}^{n} \frac{x_i \lambda_i}{\sum_{j=1}^{n} x_j \phi_{ij}} \tag{10}$$

where λ_i is the thermal conductivity of the i^{th} component, and ϕ_{ij} is defined as:

$$\phi_{ij} = \frac{[1 + \left(\frac{\mu_i}{\mu_j}\right)^{0.5} \left(\frac{M_j}{M_i}\right)^{0.25}]^2}{\sqrt{8}(1 + \frac{M_i}{M_j})^{0.5}} \tag{11}$$

where μ_i and M_i are the dynamic viscosity and the molar mass of the i^{th} component, respectively. The viscosity of the gas mixture μ_{mix} was calculated from the gas mixture composition[56]:

$$\mu_{\mathrm{mix}} = \frac{\sum_{i=1}^{n} x_i \mu_i \sqrt{M_i}}{\sum_{i=1}^{n} x_i \sqrt{M_i}} \tag{12}$$

Modeling details for first-principles-based reactor simulations

CH_4 pyrolysis was modeled using an *ab initio* gas-phase reaction mechanism[57]. This gas-phase reaction mechanism involves 501 species and 9,286 reactions that belong to six main reaction families: (1) hydrogen atom abstraction; (2) dissociation/recombination; (3) isomerization; (4)

addition/β-scission; (5) disproportionation; and (6) other reactions, such as Diels-Alder and retro-Diels-Alder reactions. The full microkinetic model was solved in a continuous stirred tank reactor using an in-house Fortran code built around the Chemkin II chemical kinetics library of subroutines[58].

The experimental results shown in Fig. 3c and 3d suggest that the CH_4 conversion affects the selectivity to various species. For a fair comparison between the two operation modes of PHQ and continuous heating, both reactors adopted the same 5% CH_4 conversion to ensure that the mechanistic study was carried out in the kinetically-controlled regime.

A temperature ramp followed by exponential decay of temperature was applied on the reactor to simulate the PHQ process under transient conditions[59], while the steady-state operation (continuous heating) of the reactor was simulated under isothermal conditions (Supplementary Figure 14b). In the case of PHQ, CH_4 pyrolysis was assumed to occur during the temperature ramp. No further reaction occurs during cooling of the gas-phase mixture, which maintains its fixed composition obtained at the end of the temperature ramp (*i.e.*, 5% CH_4 conversion).

The heat rates (Q) were calculated in the presence or absence of CH_4 pyrolysis from the energy balance:

$$Q = \rho V_r c_p \frac{dT}{dt} + \dot{m}_{in}(H_{out} - H_{in}) \quad 13$$

where ρ is the density of the reaction mixture, V_r denotes the reactor volume, c_p is the heat capacity of the reaction mixture, dT/dt denotes the differential change of temperature over time (which is zero at steady-state isothermal conditions), $\dot{m}_{in}$ is the total inlet mass flow rate, H_{out} is the total outlet enthalpy per unit mass, and H_{in} is the total inlet enthalpy per unit mass. It is worth noting that the energy balance equation is generally applicable to the entire reactor control volume, and the heat of reaction is embedded in the differences between the outlet and inlet enthalpies. Nevertheless, as seen in Supplementary Figure 16, at the set CH_4 conversion (*i.e.*, 5%) the heat of the reaction does not add significantly to the overall heat required to operate the system. This finding also allows us to perform a more extensive analysis of the heating requirements with varying pulse duration (Supplementary Figures 17, 18), avoiding the need to include the reaction (*i.e.*, by only using an inert gas flow).

We calculated the characteristic timescales for each elementary step in the reaction path of CH_4 pyrolysis toward aromatics formation (Supplementary Figure 15d). The timescales were calculated as $1/k_1$ for a unimolecular reaction and $1/(k_2[X])$ for a bimolecular reaction (where k_1 and k_2 are the rate coefficients for uni- and bi-molecular reactions at 1,500 K, respectively, [X] stands for the steady-state concentration of the depicted reactant simulated at 1,500 K, 5% CH_4 conversion, and an inlet molar ratio of CH_4:Ar equaling to 3:1). The highest temperature available by the modeling framework was selected. The upper limit of the temperature leads to the lowest timescales of the processes of interest. The fact that PHQ can enable pulse heating durations (*e.g.*, 0.02 and 0.055 s) that are shorter than the lowest reaction timescales shows the robustness of our modeling results. An analysis of forward and reverse reaction rates for each elementary step shows that the first step of CH_4 to methyl radicals (CH_3•) is close to equilibrium (with a partial equilibrium index less than 0.55) while the rest of the elementary steps in the reaction path are not equilibrated. The cyclization reaction from propargyl radicals is found to be the slowest step (red, Supplementary Figure 15d)

along the path to aromatics at the investigated conditions, with a timescale ($\tau_{cyclization}$) larger than the pulse durations (τ_{pulse}). Hence, quenching of aromatics formation can be achieved by operating the pulse duration below the timescale for this cyclization reaction.

Active learning for the CH_4 pyrolysis reaction

General discussion: Active learning is an umbrella approach for building models based on learning from experimental datasets, then proposing new experiments and using the results to improve the model's accuracy and decrease the subsequent experimental effort in finding the global optima (ref. [26]). We employed Bayesian optimization-based active learning[60,61] to help us determine the optimal C_2H_4 yield (a value-added product). To apply active learning in the PHQ system, we chose T_{high} and the pulse duration as two variables in the model that affect the C_2H_4 yield, as they can be accurately programmed in the PHQ process, and notably are unattainable by conventional methods. In the active learning loop, the first iteration of the model suggested the conditions of T_{high} = 2,000 K and pulse duration = 0.165 s (0.935 s off), which was based on where the optima were expected (red region in Fig. 3f) from the initial 23 experimental data points (white region in Fig. 3g). The C_2H_4 yield at this suggested data point (Experiment No. 25, orange region in Fig. 3g) was experimentally determined to be 11.51%. The second iteration by the active learning model then generated the conditions of T_{high} = 2,000 K and pulse duration = 0.21 s (0.89 s off), which resulted in a higher yield of 11.82% (highest in Fig. 3g, Experiment No. 28, green region in Fig. 3g). In the third iteration, the model explored conditions near T_{high} = 2,000 K and pulse duration = 0.21 s, and generated T_{high} = 2,000 K and pulse duration = 0.24 s (0.86 s off) to validate the measured optima. The experimental C_2H_4 yield at this point was 10.72% (Experiment No. 31, blue region in Fig. 3g), lower than the previous values. Therefore, we stopped iterating the model here, having found 2,000 K and 0.21 s were the optimal conditions to achieve the highest C_2H_4 yield. In addition to the aforementioned heating conditions, we also collected more data points (Experiment No. 24, 26, 27, 29 and 30) at lower temperatures guided by the model to improve its accuracy. The final dataset showed the surrogate model was accurate with an error of only 0.23% in terms of the root mean square error (RMSE) evaluated by Leave-One-Out Cross-Validation[62].

Surrogate model: For the schematic shown in Fig. 3e, the true function of the C_2H_4 yield (*i.e.*, the objective response, y) given a set of T_{high} and pulse duration (*i.e.*, independent variables, X) is unknown. We established a surrogate model using a Gaussian Process (GP) that is suitable for datasets of small to medium size such as the initial dataset containing 23 experimental data points corresponding to the white region in Fig. 3g. To locate the global optima of C_2H_4, we used q-Expected Improvement (qEI) as the acquisition function to predict where to experimentally sample the next data point (X_{next}) by changing the two variables[63]. X_{next} was chosen either to minimize the uncertainty of the model or to explore the region where the optima was expected. After performing the next experiment, the model learns from the new X and y values.

Bayesian Optimization: Bayesian Optimization is a machine learning-based algorithm that aims to maximize the desired objective function[63,64]. The method performs well on small to medium sized data and requires a continuous objective function on the domain of interest. It is especially useful when the maximized function has no known particular structure, such as convexity. There are two parts to the algorithm: first, the Bayesian statistical model needed to construct the surrogate model; second, the acquisition function required to decide where to sample in the domain of interest. The surrogate model is built on the training data set. Based on the model predictions, the acquisition

function samples points to minimize the uncertainty in predictions ('explore') or accurately predict the optimum ('exploit'). The sampled point is evaluated using the objective function (in cases where there is no function, an experiment is run), and the surrogate model is re-trained on the new data. This procedure is repeated until the desired accuracy or an optimum value is reached.

Gaussian process: GP regression is the used data-driven approach for building the surrogate model[65]. Let f be the objective function (in cases where there is no f, f is replaced by the experiment) and x_1, $x_2 \ldots x_k$ be the training data points on which we perform the experiments. In a Gaussian process regression, we assume that $[f(x_1), f(x_2), \ldots f(x_k)]$ is drawn from a multivariate normal distribution known as the prior. The mean vector is constructed by evaluating a mean function $\mu_0(x)$ at each observation x_i and the covariance matrix is constructed by evaluating a kernel function Σ_0 at each pair of points (x_i, x_j):

$$[f(x_1), f(x_2), \ldots f(x_k)] \sim Normal(\mu_0(x_{1:k}), \Sigma_0(x_{1:k}, x_{1:k})) \quad (14)$$

Here $x_{1:k}$ represents the k experimental points vector, on which the mean and covariance functions are applied, to generate the mean vector and covariance matrix, respectively. To make predictions on a new data point x, the following distribution is evaluated using Bayes Rule:

$$f(x)|[f(x_1), f(x_2), \ldots f(x_k)] \quad (15)$$

This distribution is known as the posterior conditional distribution.

In this work, we have modeled C_2H_4 yield ($f(x)$) to be a bivariate normal distribution on the pulse duration (x_1) and T_{high} (x_2) using a Matern Kernel.

Acquisition function: Expected Improvement is the acquisition function used in our Bayesian Optimization[64,66]. It offers a closed-form solution when applied on a Gaussian posterior conditional distribution and is inexpensive to evaluate.

Let x_{new} be the new point to be sampled, and $f*$ be the maximum value observed so far. The goal of the acquisition function is to choose x such that the expectation of the difference between the posterior conditional distribution evaluated at x and the best value is maximized. The maximized Expected Improvement is described using the following equation:

$$max\ EI\left(\left[f_p(x_{new}) - f*\right]_+\right) \quad (16)$$

where $f_p(x)$ is the posterior distribution. This optimization has a closed-form solution for a Gaussian posterior and can be found using integration by parts, followed by a gradient-based maximization. The Expected Improvement is maximized both for a high-quality observation (near the optimum) and a highly uncertain observation (in the region which has not been sampled before). A common occurrence is that once the Expected Improvement function samples a point which is the best value seen by the model, the function samples near it to fine-tune the optima ('exploit').

In this work, we use q-Expected Improvement as the acquisition function, which is a variant of the Expected Improvement[63]. Instead of evaluating the integral using integration by parts, we use Monte-Carlo-based sampling and evaluate the integral as a summation. This is especially useful for surrogate models where the integral is not analytically tractable.

Multi-objective Optimization: The PHQ process can also be driven by active learning to further optimize the yield of multiple products due to its greater tunability than continuous heating. Active

learning is used to perform multi-objective optimization to simultaneously maximize the primary product yield and minimize side product formation (two objectives), and to reduce downstream separation costs. For example, with this approach we observed a Pareto front behavior[67] when simultaneously maximizing the C_2H_4 yield and minimizing the undesired product yield (*i.e.*, benzene and naphthalene).

The multi-objective optimization framework is shown in Supplementary Figure 13a. We first constructed 2 Gaussian process models, GP_{Y_1} and GP_{Y_2}, to predict the C_2H_4 yield and the undesired benzene and naphthalene product yield, respectively, for the given experimental dataset. We then constructed a Gaussian process model on the experimental dataset, GP_Y, which maps the pulse duration and T_{high} to the modified response variable at each w, Y_{mod}. This model is assumed to be the ground truth for the chosen w. Our aim was to find the pulse duration and T_{high} that maximize GP_Y. As Gaussian process models are kernel methods, we maximized GP_Y by appropriate sampling. To do so, we constructed another Gaussian process surrogate model on the assumed ground truth model. To train the surrogate, we sampled 10 points from the pulse duration and T_{high} search space using a Latin Hypercube Sampling design and found the corresponding Y_{mod} using GP_Y. We sampled the pulse duration and T_{high} data points in the defined search space to maximize the Expected Improvement acquisition function, evaluated on the surrogate model. The Y_{mod} for the sampled point was calculated using the GP_Y, and the surrogate model was then conditioned on the new data point. This procedure was repeated until the best value seen by the surrogate was the same for five consecutive iterations (~30 iterations of the procedure). The pulse duration and T_{high} that corresponds to the maximum were then passed onto GP_{Y_1} and GP_{Y_2} to evaluate the C_2H_4 yield and the undesired product yield, respectively.

Supplementary Figures 13b and 13c indicate a positive relationship between the C_2H_4 yield and the undesired product with a Pearson correlation coefficient of 0.829 and a Pareto optimal front[68]. The Pareto front captures the trade-off between maximizing the C_2H_4 yield and minimizing the undesired product yield. The objective function (Y_{mod}) is modified in a form to reflect the contribution from both objectives[67,69]:

$$Y_{mod} = w \times Y_1 - (1 - w) \times Y_2 \quad (17)$$

where w is the weight assigned to each objective function and $w \in [0,1]$, Y_1 is the C_2H_4 yield, and Y_2 is the undesired product yield. To construct the Pareto front, we discretized w and maximized Y_{mod} for each value of w to capture the tradeoff between the two objectives. To minimize the formation of undesired products at a targeted C_2H_4 yield, we constructed a response that maximized the negative of the undesired products yield (the negative sign in front of the second term), with the detailed learning process illustrated in Supplementary Figure 13a.

Modeling details for the migration of Ru-H and Fe-H and the self-healing of carbon defects

The carbon support was modeled by a supercell of a single graphene layer containing 32 carbon atoms. Defects in the carbon support were used to strongly anchor metal atoms in the model while studying metal atom migration under high temperatures. A vacuum gap of 15 Å and a dipole correction was included to separate subsequent graphene slabs. Spin-polarized periodic density functional theory (DFT) calculations were performed using the Vienna Ab initio Simulation Package (VASP)[70-73] and the projector-augmented wave (PAW) method[74,75]. The exchange-correlation energies were calculated on the basis of the generalized gradient approximation (GGA) according to Perdew and Wang (PW91)[75,76]. The plane-wave energy cutoff was set to 400 eV,

while the Brillouin zone was sampled using a 5 × 5 × 1 Γ-centered k-point mesh. A maximum force convergence criterion of 0.05 eV $Å^{-1}$ was used and each self-consistency loop was iterated until a convergence level of 10^{-6} eV was achieved. Transition state search was performed using nudged elastic band and dimer calculations[77,78]. The nudged elastic band method was used to find an initial guess for the minimum energy path, which was used as a starting point for dimer calculations. Characteristic timescales were calculated using the following equation based on the transition state theory[79,80]:

$$\tau = \frac{1}{k} = \frac{he^{(\Delta E^{\ddagger}/RT)}}{k_B T} \quad 18$$

where τ is the characteristic timescale, k is the rate coefficient from transition state theory, h is the Planck constant, $\Delta E^{\ddagger}$ is the activation barrier as calculated by DFT, R is the gas constant, k_B is the Boltzmann constant, and T is the temperature. The characteristic timescales for the migration of Ru-H and Fe-H and the self-healing of carbon defects were all calculated using a temperature of 1,300 K. Note that T_{high} of the PHQ process (*e.g.*, 1,300 K) was selected for modeling the timescales. According to Equation 18, the upper limit of the temperature leads to the lowest timescales of the processes of interest. The fact that PHQ can enable pulse heating duration (*e.g.*, 0.11 s) that is shorter than the lowest timescales shows the robustness of our modeling results.

Microkinetic modeling of NH_3 synthesis

The NH_3 synthesis was simulated in the 0-D homogeneous module of CHEMKIN software[81]. A recently developed HP mechanism[82] with nitrogen-containing library[83,84] was used in the gas-phase model. A surface-based mechanism by Bowker *et al.* (ref. [34]) was used to predict the NH_3 production on the catalyst surface. All seven-step reversible surface reactions in the Haber-Bosch process were considered in the surface-based mechanism.

The model employed a simulated temperature profile, where a temperature ramp followed by an exponential decay of temperature was applied on the reactor to simulate the PHQ process under non-equilibrium conditions. The steady-state operation (continuous heating) of the reactor was simulated under isothermal conditions. The surface site density of the pristine catalyst was estimated as 1×10^{-9} mol/cm^2. The surface site density of the used catalyst after 1 h operation by both methods was calculated by multiplying the original surface site density with the percentage change of average surface area of the nanoparticles after the reaction, assuming all the nanoparticles are spherical (Fig. 4d and 4e).

Supplementary Table 1

Electrical parameters used for heating the carbon paper at various conditions.

Pulse Duration (s)	Peak Temperature (K)	Applied Voltage (V)
0.02	1,200	~55
0.02	1,400	58~61
0.02	1,600	61~64
0.02	1,800	64~67
0.02	2,000	67~72
0.055	1,200	28~33
0.055	1,400	33~35
0.055	1,600	35~37
0.055	1,800	~38
0.055	2,000	38~40
0.11	1,200	~26
0.11	1,400	26~28
0.11	1,600	28~30
0.11	1,800	~30
0.11	2,000	30~33
0.33	1,200	~16
0.33	1,400	16~18
0.33	1,600	18~20
0.33	1,800	20~22
0.33	2,000	~24

Supplementary Table 2

Geometrical parameters used in the numerical model.

Model Component	Shape	Dimensions
Carbon paper	Square prism	20 mm × 8 mm × 0.21 mm
Quartz tube	Cylinder	Diameter = 10 mm, Length = 40 mm

Supplementary Table 3

Properties of the materials used in the numerical model.

Materials	Specific heat capacity (J/mol•K)	Thermal conductivity (W/m•K)	Density (kg/m^3)	Emissivity	Viscosity
Carbon paper	ref. [19]	10 (parallel) 0.2 (perpendicular) SI ref. 44-47	452	0.95, SI ref. 48	N/A
Quartz tube	N/A	N/A	N/A	0.75	N/A
Methane gas	SI ref. 49	SI ref. 50	Ideal gas law	0	SI ref. 51
Argon gas	20.813	SI ref. 52	Ideal gas law	0	SI refs. 53,54

Supplementary Discussion 1

The PHQ reactor can be simply modified from a conventional flow reactor setup (Supplementary Figure 1). The carbon heater is placed in a quartz tube (1/2" outer diameter) and connected to a power source *via* copper wires that are protected by alumina ceramic tubes. At both ends of the reactor, we attach Swagelok Ultra-Torr tee fittings, in which one port of each tee is used for the electrical connection, and the other is used for the gas inlet or outlet.

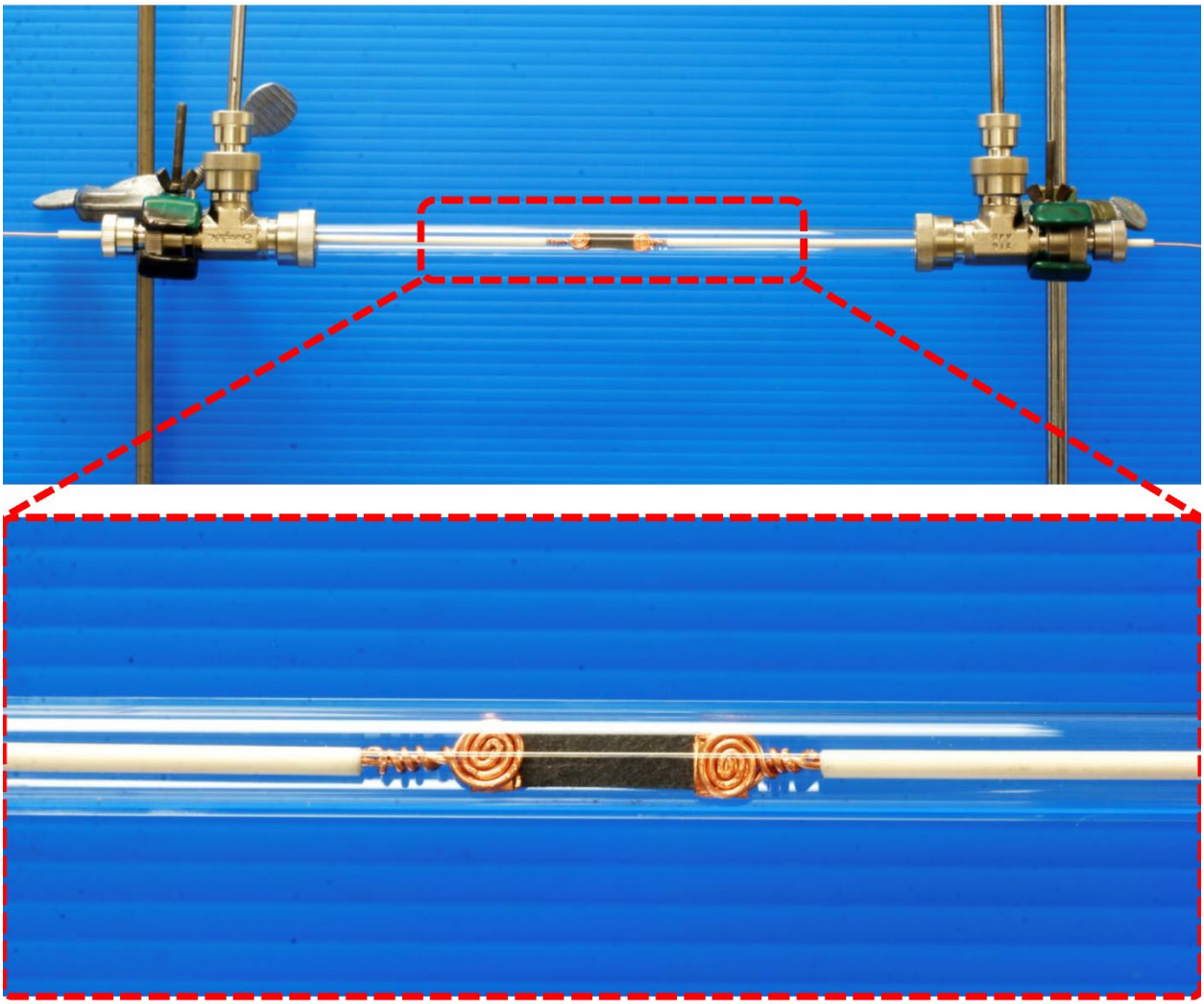

Supplementary Figure 1. Digital images of the PHQ reactor.

The schematic drawing of the electrical circuit is shown in Supplementary Figure 2. The input signal is passed from the sourcemeter to the solid-state relay device, which provides the ability to program the on/off switching. The output signal of the solid-state relay is applied to the power source and the reactor, which are connected in series. The pulse peak temperature (T_{high}) is controlled by the electrical power of the power source, while the pulse duration is controlled by the "on" duration of the sourcemeter.

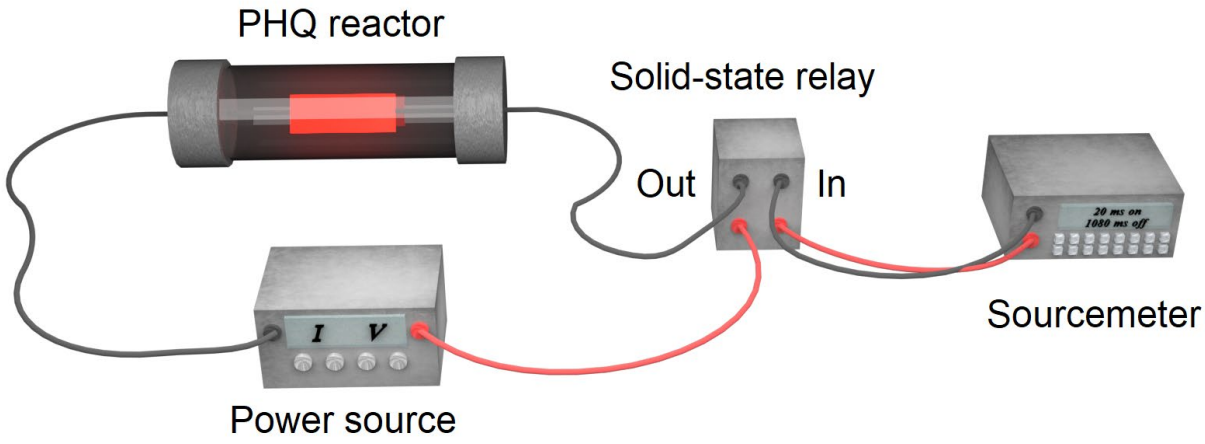

Supplementary Figure 2. Schematic drawing of the electrical circuit.

Supplementary Discussion 2

An electric current is applied through the carbon paper to generate heat. We are able to achieve ramping and cooling rates of ~10^4 K/s owing to the low heat capacity of the carbon paper heater. Notably, Joule heating of the carbon paper heater can allow us to reach ~2,400 K in milliseconds. After turning off the power, the heater quickly cools down to ~800 K within ~1s (Supplementary Figure 3).

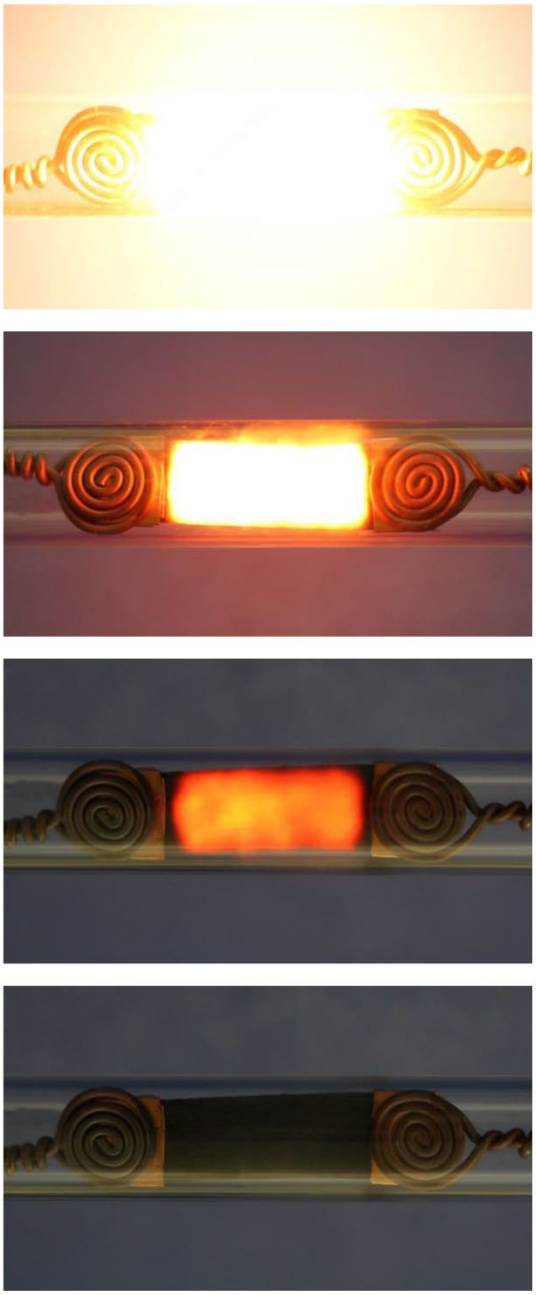

Supplementary Figure 3. Four selected frames from a recorded video during the cooling process of the carbon paper heater.

Supplementary Discussion 3

For the CH_4 pyrolysis reaction, the high temperature of the carbon paper heater exponentially increases the reaction rate for high CH_4 conversion, without the need of using additional catalysts. As shown in Supplementary Figure 4, the surface of the carbon paper heating element is catalyst-free.

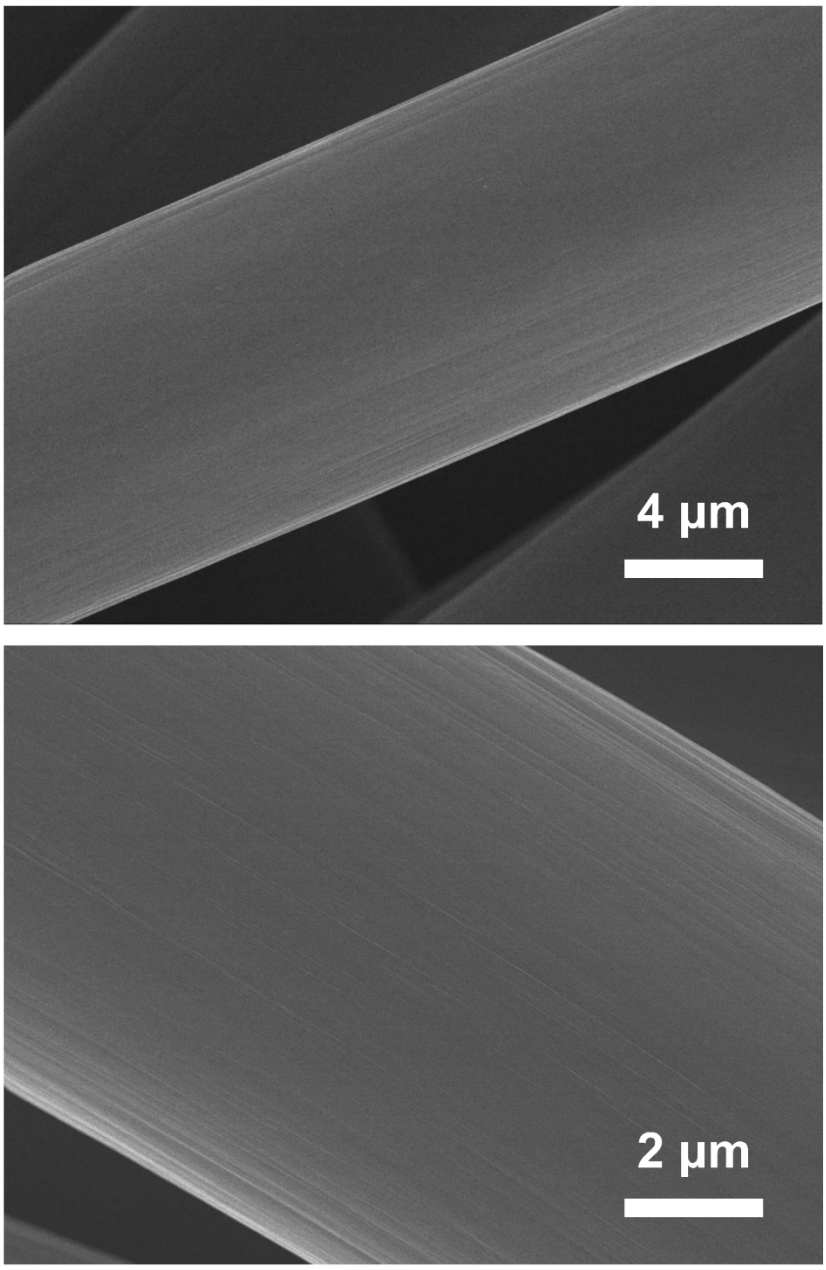

Supplementary Figure 4. SEM images of the carbon paper heater at different magnifications.

Supplementary Discussion 4

Supplementary Figure 5 showcases the flexibility of the carbon paper as a model heating element used in this work for the PHQ operations. The structural flexibility of the carbon heater provides the potential to manipulate its shape for enhanced interaction with the gas molecules for spatial tunability of the temperature.

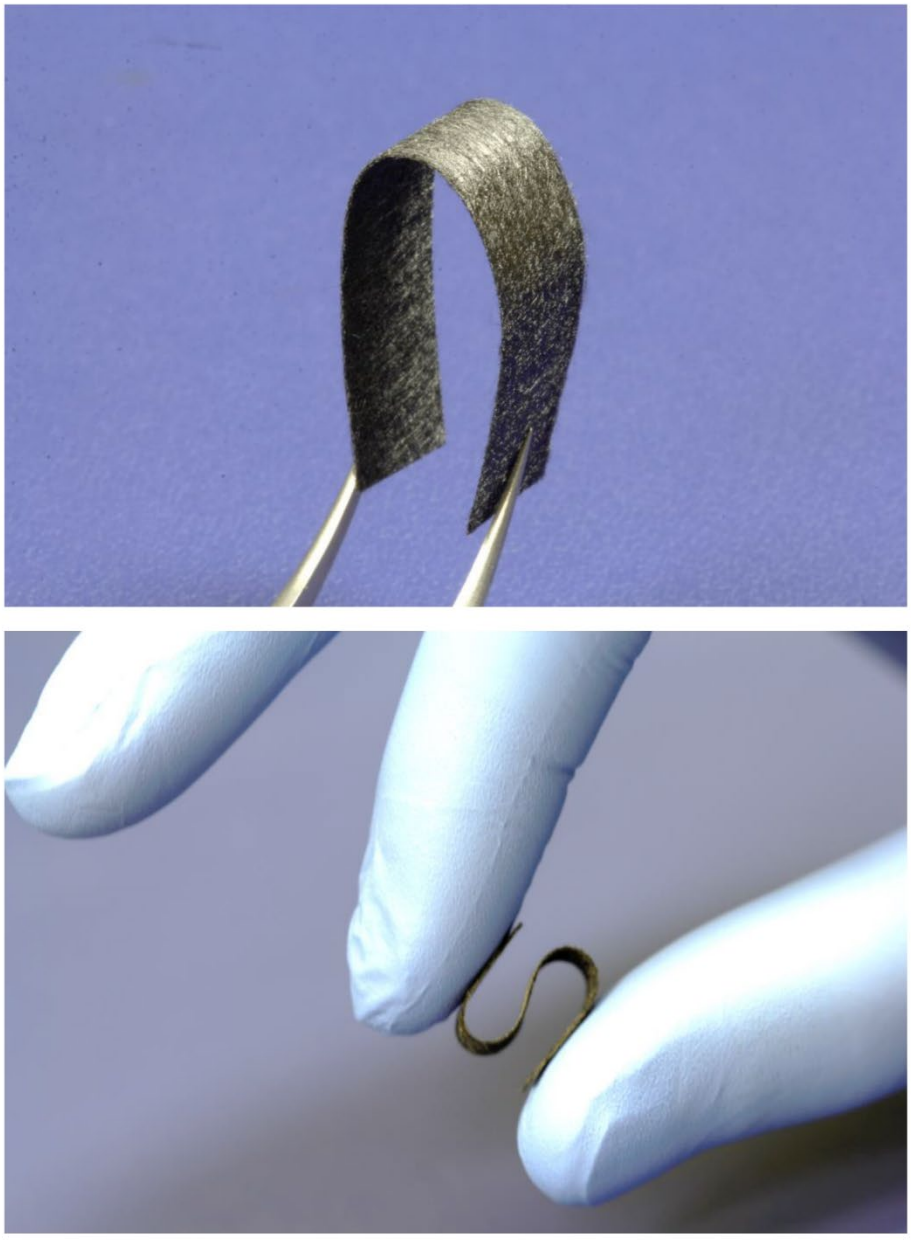

Supplementary Figure 5. Digital images of the flexible carbon paper heater with various configurations.

Supplementary Discussion 5

An example of the peak temperature (T_{high}) measurement is shown in Supplementary Figure 6. The temperature distribution is captured using a high-speed camera. We convert the color image (on the left) of the carbon heater to a temperature map (on the right) to extract the average temperature (~2,500 K) throughout the material. The slight temperature variation at different positions of the carbon paper heater is due to the presence of pores of the material.

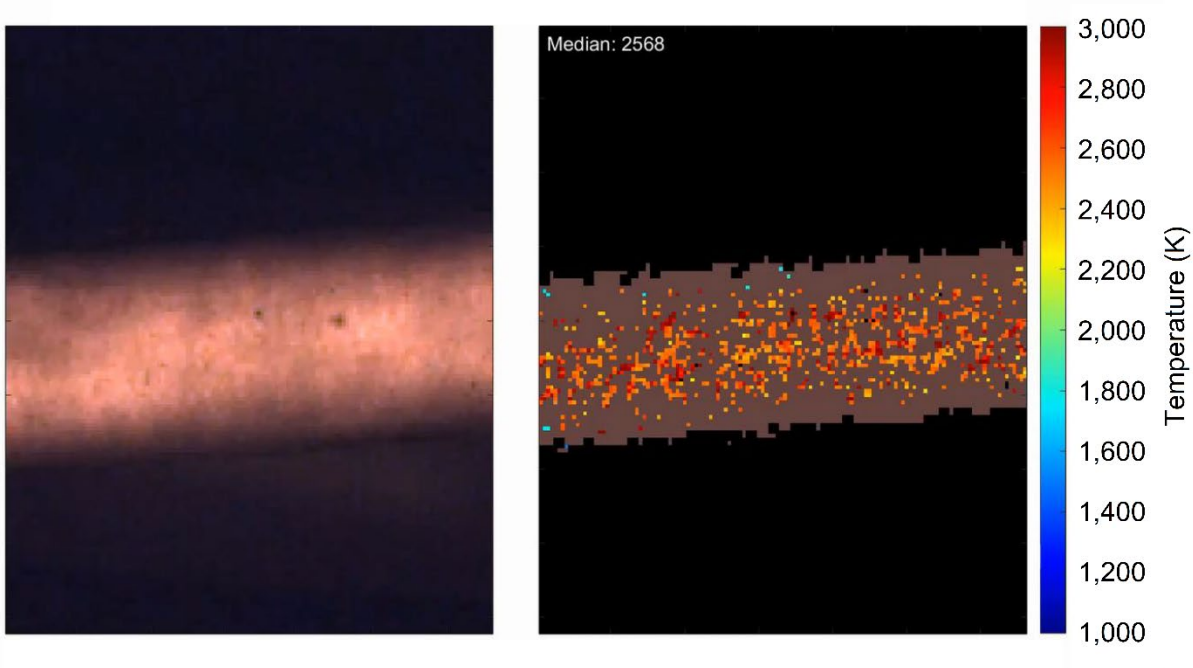

Supplementary Figure 6. Peak temperature (T_{high}) measurement using a high-speed camera.

Supplementary Discussion 6

We use numerical simulations to verify the temperature profile of the gas molecules. The gas molecules interact closely with the carbon paper heater, therefore their temperature profile coincides with that of the heater precisely. Supplementary Figure 7 shows the heater (measured) and gas temperature (simulated) in the PHQ system with T_{high} of 1,800 K. The three traces shown in Supplementary Figure 7b represent the temporal temperature patterns of three spatial positions (in the reactor cross-section) vertically above the middle point on the upper surface of the carbon paper with distances (d) of 0R', 1/16R', and 1/8R' (R' is the closest distance from the middle point on the upper surface of the carbon heater to the edge of the cylindrical reactor, R'=R-1/2D, where R is the radius of the cylindrical reactor and D is the thickness of the carbon paper).

Supplementary Figures 8 and 9 demonstrate the rapid heating and cooling rates using the cross-sectional contour images of the gas temperature distribution at various times on stream. These results confirm that our PHQ method enables an accurate, temporal temperature pattern experienced by the gas molecules flowing through the reactor and interacting with the carbon heater.

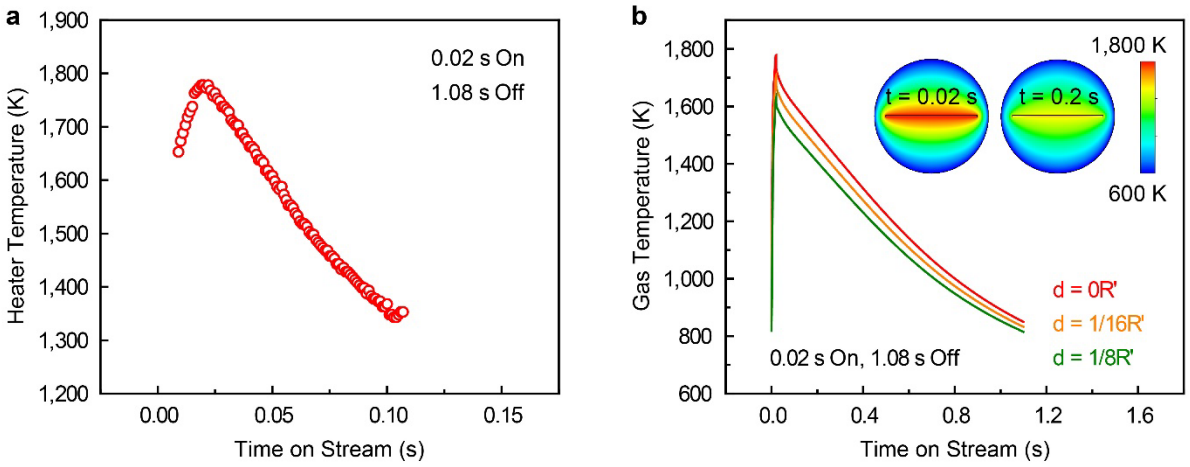

Supplementary Figure 7. Heater and gas temperatures in the PHQ system. (a) The measured temperature profile of the carbon paper heater, replotted from Fig. 2e. (b) Numerical simulation demonstrates the temperature profile of the gas molecules closely follows that of the carbon heater, as showcased using a typical pulse duration of 0.02 s over 1.1 s and a T_{high} of 1,800 K. The insets show the cross-sectional contour images of the gas temperature distribution when the time on stream equals 0.02 s and 0.2 s in a pulse period (0.02 s on, 1.08 s off).

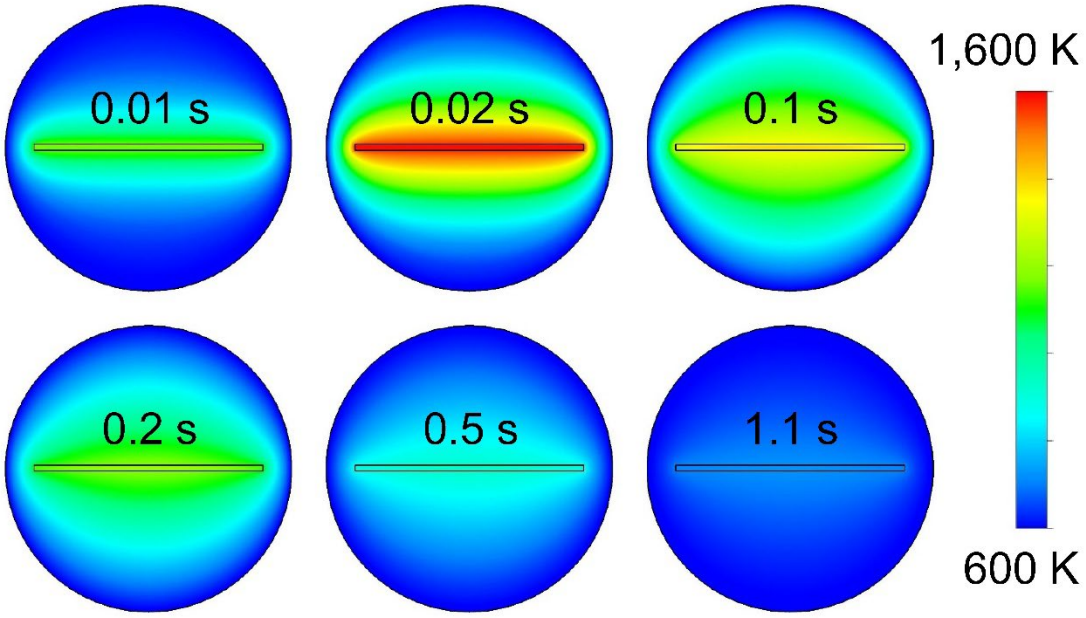

Supplementary Figure 8. Cross-sectional contour images of the gas temperature distribution when the time on stream equals 0.01 s, 0.02 s, 0.1 s, 0.2 s, 0.5 s, and 1.1 s in a pulse period (0.02 s on, 1.08 s off; T_{high} = 1,600 K). The temperature of the gas near the surface of the carbon paper (whose geometry is not optimized) follows closely to that of the heating element.

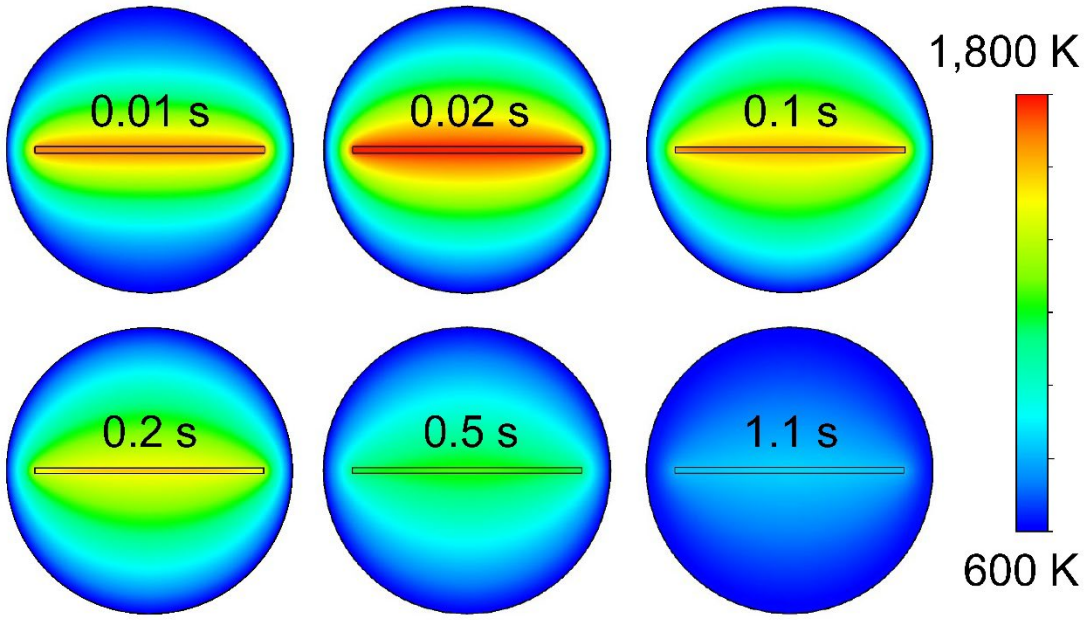

Supplementary Figure 9. Cross-sectional contour images of the gas temperature distribution when the time on stream equals 0.01 s, 0.02 s, 0.1 s, 0.2 s, 0.5 s, and 1.1 s in a pulse period (0.02 s on, 1.08 s off; T_{high} = 1,800 K). The temperature of the gas near the surface of the carbon paper (whose geometry is not optimized) follows closely to that of the heating element.

Supplementary Discussion 7

As shown in Supplementary Figure 10, the CH_4 conversion and C_2 product selectivity remain relatively stable during the PHQ operation. In particular, the selectivity to coke remains low (< 5%). In this experiment, we used a T_{high} of ~2,000 K, a pulse duration of 0.055 s over a period of 1.1 s (0.055 s on, 1.045 s off), and a flow rate of 20 sccm (75 mol% CH_4, 25 mol% Ar). The dimensions of the carbon paper used for this experiment were 40 mm × 8 mm in size, with 10 mm × 8 mm exposed during the PHQ operations, with the remaining distance at each end being wrapped with copper foil.

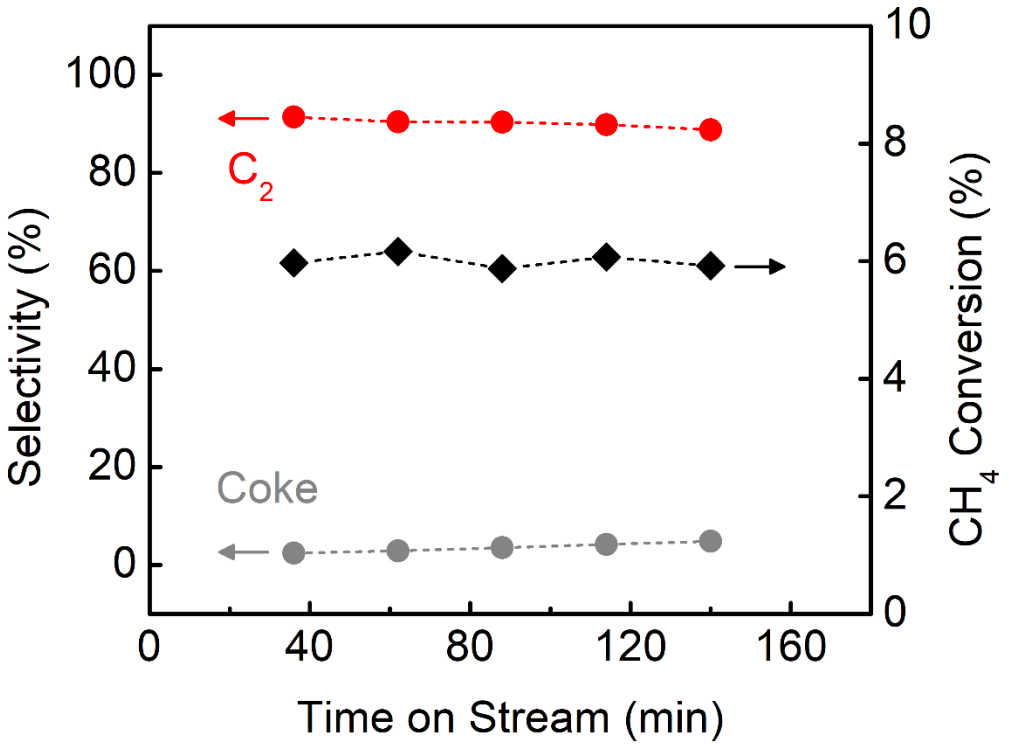

Supplementary Figure 10. CH_4 conversion and C_2 product selectivity by PHQ as a function of the time on stream.

Supplementary Discussion 8

Supplementary Figure 11 schematically showcases the programmable control of the PHQ technique, which allows us to precisely tune the pulse peak temperature (T_{high}) and pulse duration *via* the electrical signal applied to the carbon heater. Note that due to the gradual change of defect level and crystallinity of the carbon heaters (*e.g.*, carbon paper and carbon felt) during PHQ operations, the power input may need to be adjusted to maintain the desired peak temperature.

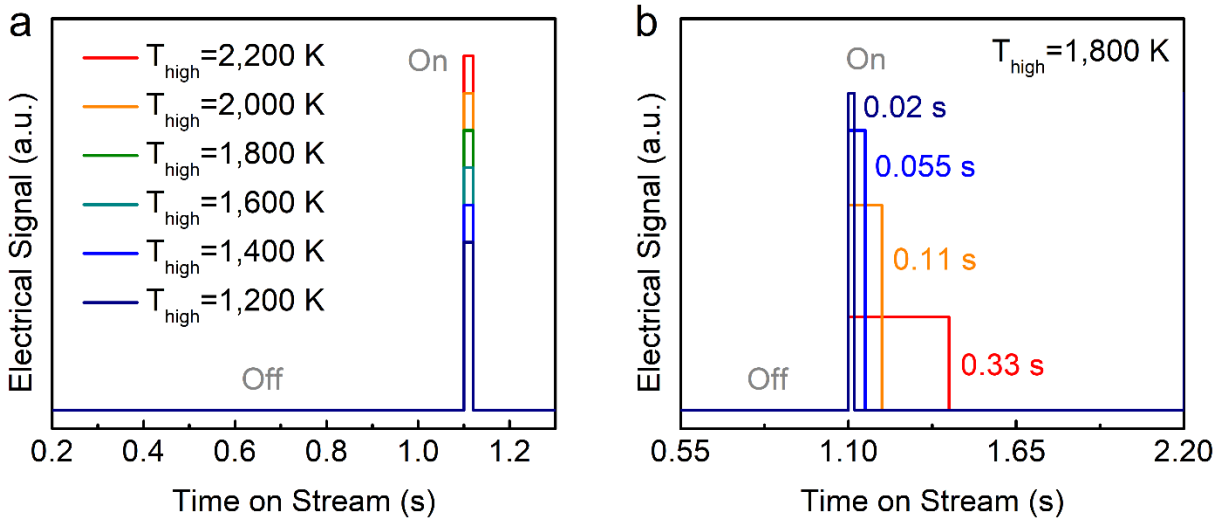

Supplementary Figure 11. Programmable control by the PHQ technique. (a) Programmable control over the peak temperature (T_{high}) from 1,200 K to 2,200 K by PHQ. (b) Programmable control over the pulse duration from 0.02 s to 0.33 s by PHQ.

Supplementary Discussion 9

Through three iterations in the active learning loop, we found T_{high} = 2,000 K and pulse duration = 0.21 s were the optimal conditions to achieve the highest C_2H_4 yield (11.82%) in our experiments, corresponding to the green dot shown as Iteration 2. Supplementary Figure 12 shows a magnified view of Fig. 3f of the main text, with a focus on the high yield region.

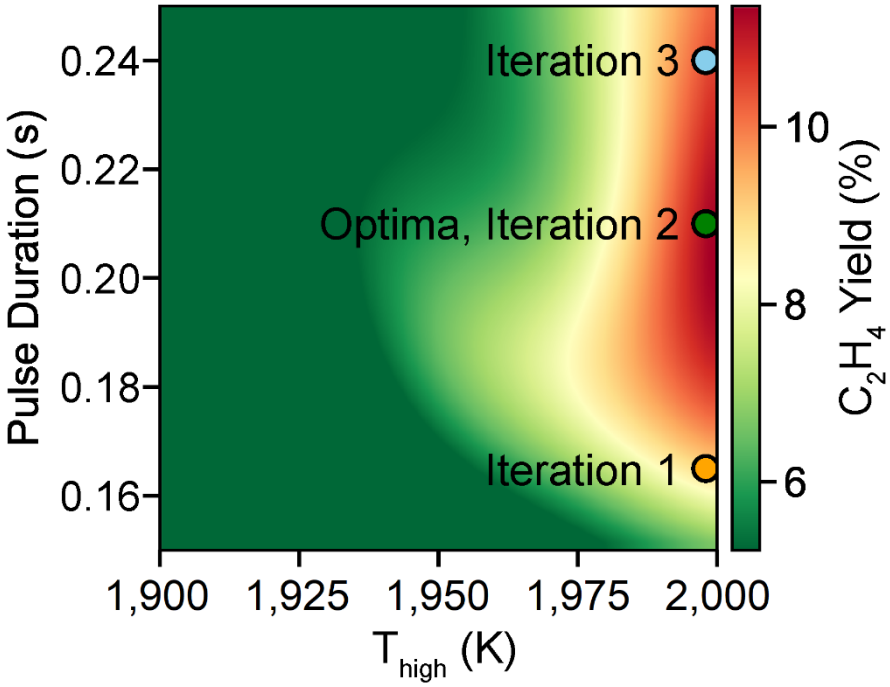

Supplementary Figure 12. Magnified view of Fig. 3f of the main text, with a focus on the high yield region.

Supplementary Discussion 10

The PHQ process can be driven by active learning to further optimize the yield of multiple products due to its greater tunability than continuous heating. As shown in Supplementary Figure 13, we applied active learning and observed a Pareto front behavior when simultaneously maximizing the C_2H_4 yield and minimizing the undesired product yield (*i.e.*, benzene and naphthalene). These results can teach us how to program the heating pattern to lower the undesired product yield at a given C_2H_4 yield (desired), or other target performance with minimal experimental effort.

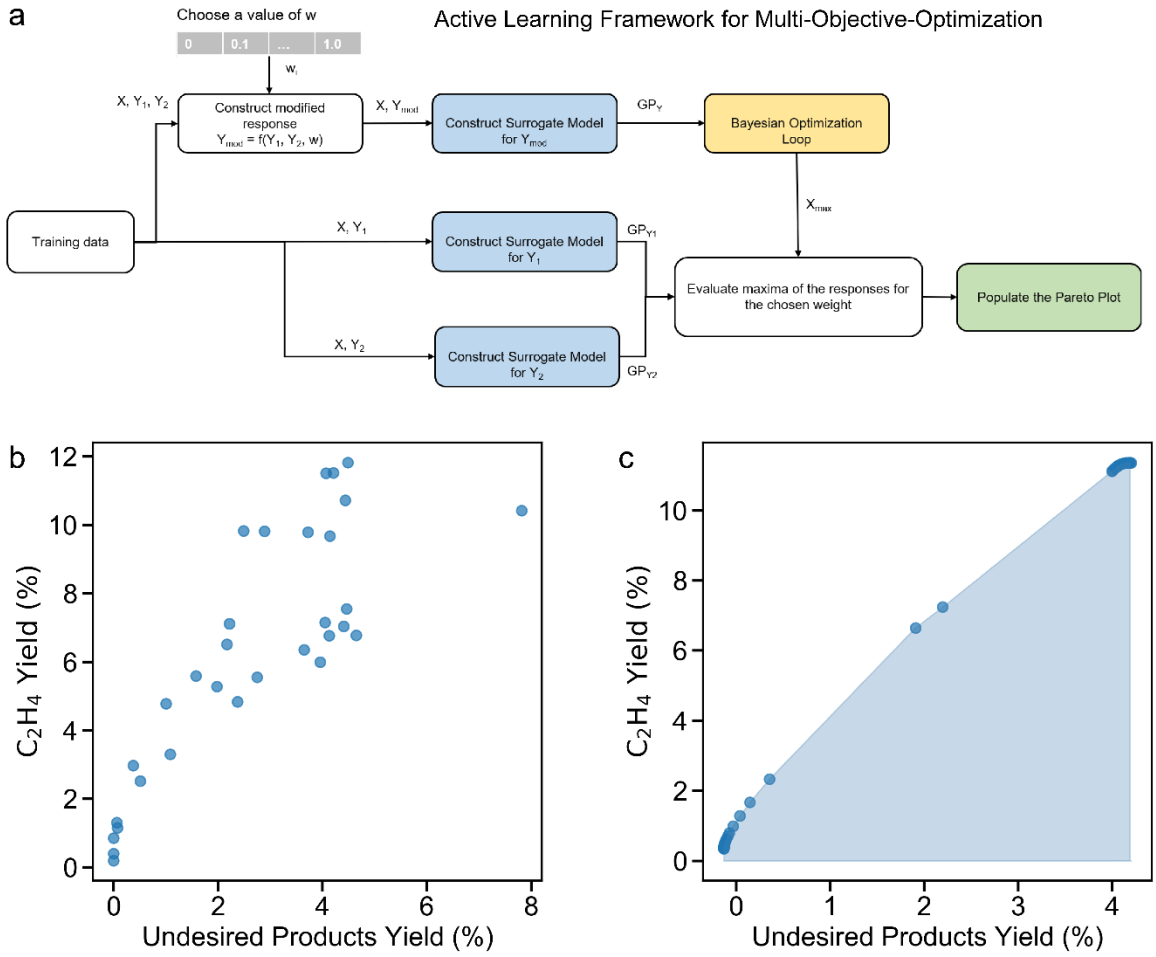

Supplementary Figure 13. Multi-objective-optimization by active learning. (a) Active learning framework for the construction of the Pareto plot. (b) Experimentally evaluated C_2H_4 yield *vs.* undesired products yield (*i.e.*, benzene and naphthalene). Conditions that increase the C_2H_4 yield also increase the undesired products yield. As a result, there is a trade-off between maximizing the C_2H_4 yield and minimizing the undesired product yield. (c) The Pareto plot shows the maximum C_2H_4 yield that can be produced for a minimum yield of undesired products. The shaded area indicates the feasible region that can be experimentally achieved.

Supplementary Discussion 11

For our first-principles-based microkinetic simulations, we modeled two types of reactors operated at steady-state (*i.e.*, under an isothermal condition) and transient modes (*i.e.*, using a rapid temperature ramp followed by an exponential decay) to simulate continuous heating and PHQ[57-59], respectively, as shown in Supplementary Figure 14. We hypothesize that the rapid heating and quenching of PHQ (red curve in b) provide a greater degree of control over the reaction pathways by matching the timescales of intermediate C_2 species formation in the CH_4 pyrolysis reaction network, but without allowing steady-state to be reached that would lead to secondary and subsequent products.

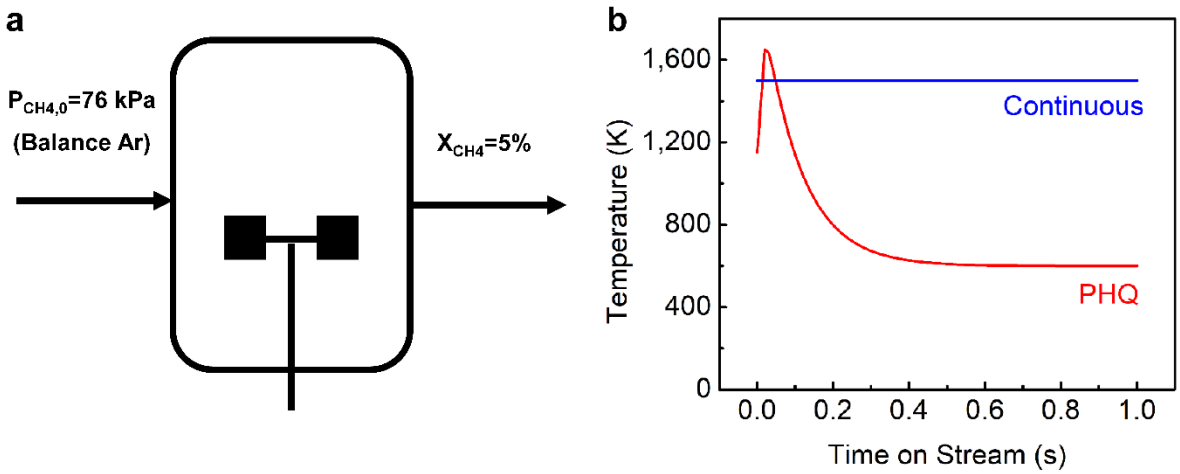

Supplementary Figure 14. Modeling details. (a) The continuous stirred tank reactor setup used to model both the continuous heating and PHQ methods. (b) Temporal temperature profiles used for the steady-state and transient reactors, simulating conventional continuous heating and PHQ, respectively.

Supplementary Discussion 12

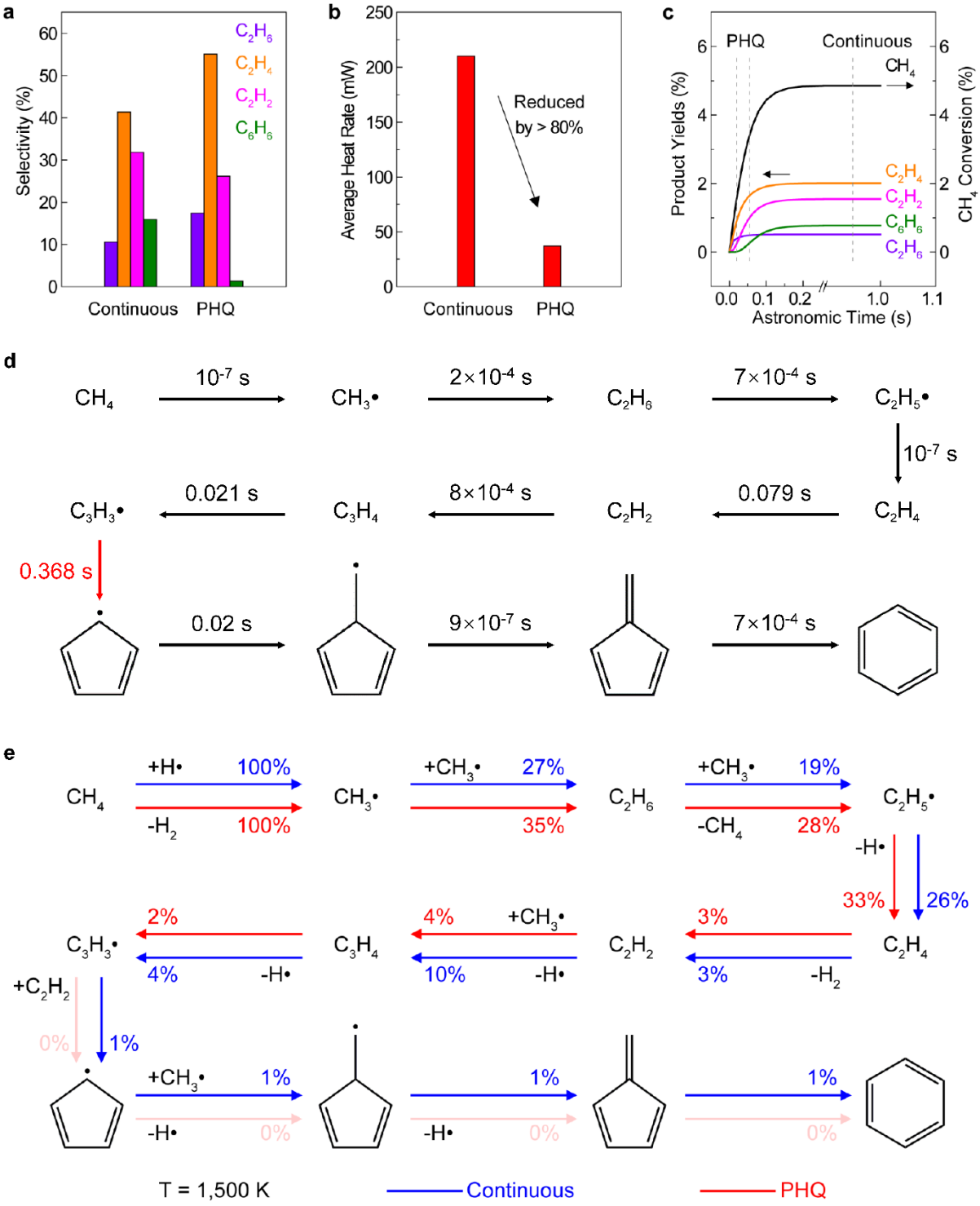

Supplementary Figure 15. Modeling of CH_4 pyrolysis reactions under continuous heating and PHQ. Comparison of the (a) product distribution and (b) energy required by the CH_4 pyrolysis reaction between steady-state (simulating continuous heating) and transient (simulating PHQ) operations at an identical CH_4 conversion of 5%. (c) CH_4 conversion and product distribution as a

function of astronomic time (*i.e.*, clock time or external time of the system) under isothermal conditions at 1,500 K. (d) Characteristic timescales for each elementary step in the reaction path of CH_4 pyrolysis toward aromatics formation, simulated at 1,500 K. The side species are omitted for clarity. The timescale for the slowest step ($\tau_{cyclization}$ = 0.368 s) along this reaction path is indicated in red. (e) Reaction pathway analysis for CH_4 pyrolysis by steady-state (blue) and transient (red) operations under isothermal conditions at 1,500 K. The percentages, next to each elementary step, correspond to the net reaction rates normalized by the net reaction rate of the initial dehydrogenation (initial CH_4 activation step) from CH_4 to CH_3•. For PHQ, the secondary and subsequent reactions after the propargyl radical (C_3H_3•) are quenched (the shaded arrows), therefore yielding more C_2 products.

We employed first-principles-based microkinetic simulations to compare the continuous heating and PHQ methods for their product distribution and energy cost. Compared with continuous heating, PHQ offers higher selectivity to C_2H_6 and C_2H_4 and lower selectivity to C_2H_2 and C_6H_6 (Supplementary Figure 15a). In addition, our calculations also show that PHQ reduces the average energy needed by > 80% compared to continuous heating at identical CH_4 conversion (Supplementary Figure 15b). Furthermore, through simulating the characteristic trajectories of CH_4 conversion and product yields up to C_6H_6 as a function of the astronomic time (Supplementary Figure 15c), we found that the transient pulse durations by PHQ (*e.g.*, 0.02 s and 0.055 s) can provide enough thermal energy to drive the CH_4 pyrolysis reaction to C_2 species but quench it before a large fraction of C_6H_6 is produced as the reaction reaches steady-state.

We calculated the characteristic timescales (Supplementary Figure 15d) and the reaction flux under PHQ and continuous heating conditions (Supplementary Figure 15e) for each elementary step in the reaction path of CH_4 pyrolysis toward aromatics formation. The results show that quenching of aromatics formation can be achieved by operating the pulse heating duration below the timescale for the cyclization reaction from C_3H_3• (red, Supplementary Figure 15d). In addition, the timescale for C_2H_2 formation from C_2H_4 is comparable to the pulse heating durations, which corroborates with the reduction in C_2H_2 formation by PHQ (Supplementary Figure 15a). Meanwhile, the timescales of the elementary steps towards C_2H_4 formation are much smaller than the pulse duration, allowing the reaction to proceed towards C_2H_4 by PHQ (Supplementary Figure 15a). The calculated reaction flux under PHQ condition is distributed in reactions among C_2 species (red, Supplementary Figure 15e), and the cyclization reaction from C_3H_3• is insignificant. In contrast, under steady-state (continuous heating) condition, the reaction flux is more uniformly distributed among all the simulated elementary steps of CH_4 pyrolysis, allowing the recombination of C_3H_3• to form aromatic species (blue, Supplementary Figure 15e).

Supplementary Discussion 13

Our energy balance calculations show that PHQ reduces the average energy needed by > 80% compared to continuous heating at identical CH_4 conversion, due to the use of a much lower average temperature. Supplementary Figure 16 suggests that the heat required by the CH_4 pyrolysis reaction is a small contribution to the total system energy needed at relatively low CH_4 conversion (*i.e.*, 5%). This result allows us to perform further analysis with an inert gas (*i.e.*, N_2) as a feed to compare the energy efficiency of continuous heating and PHQ, which can be generalized for other reaction schemes (*e.g.*, NH_3 synthesis). The results (Supplementary Figures. 17 and 18) indicate that PHQ with pulse durations of less than 0.33 s can largely reduce the required energy compared to continuous heating, potentially leading to better energy efficiency.

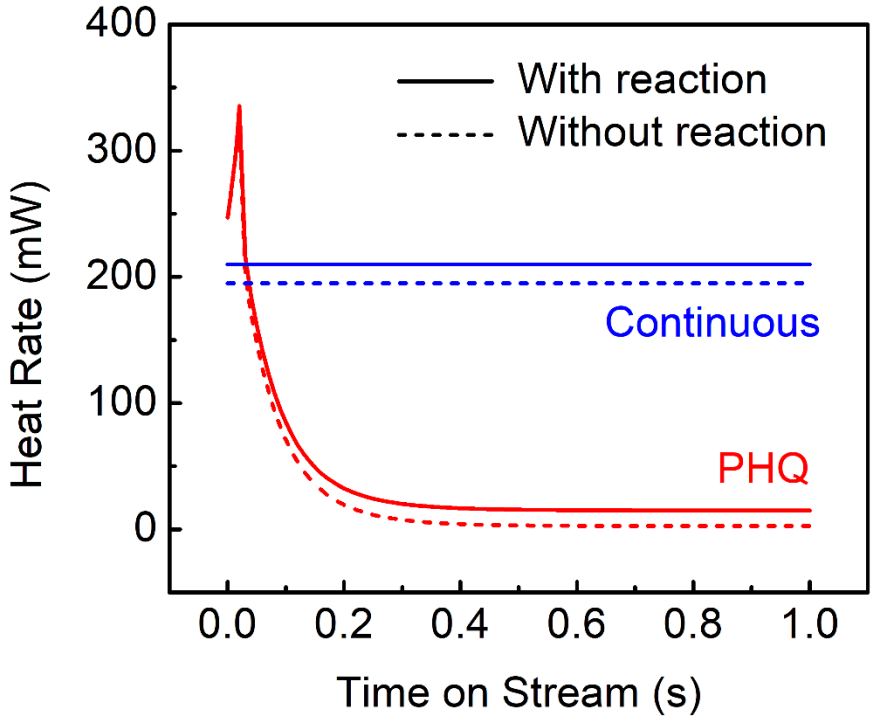

Supplementary Figure 16. Heat rate profiles for the steady-state and transient reactors, simulating conventional continuous heating and our PHQ method, respectively. The heat of the reaction constitutes only a small portion of the overall heat required to operate the system at the set CH_4 conversion of 5%.

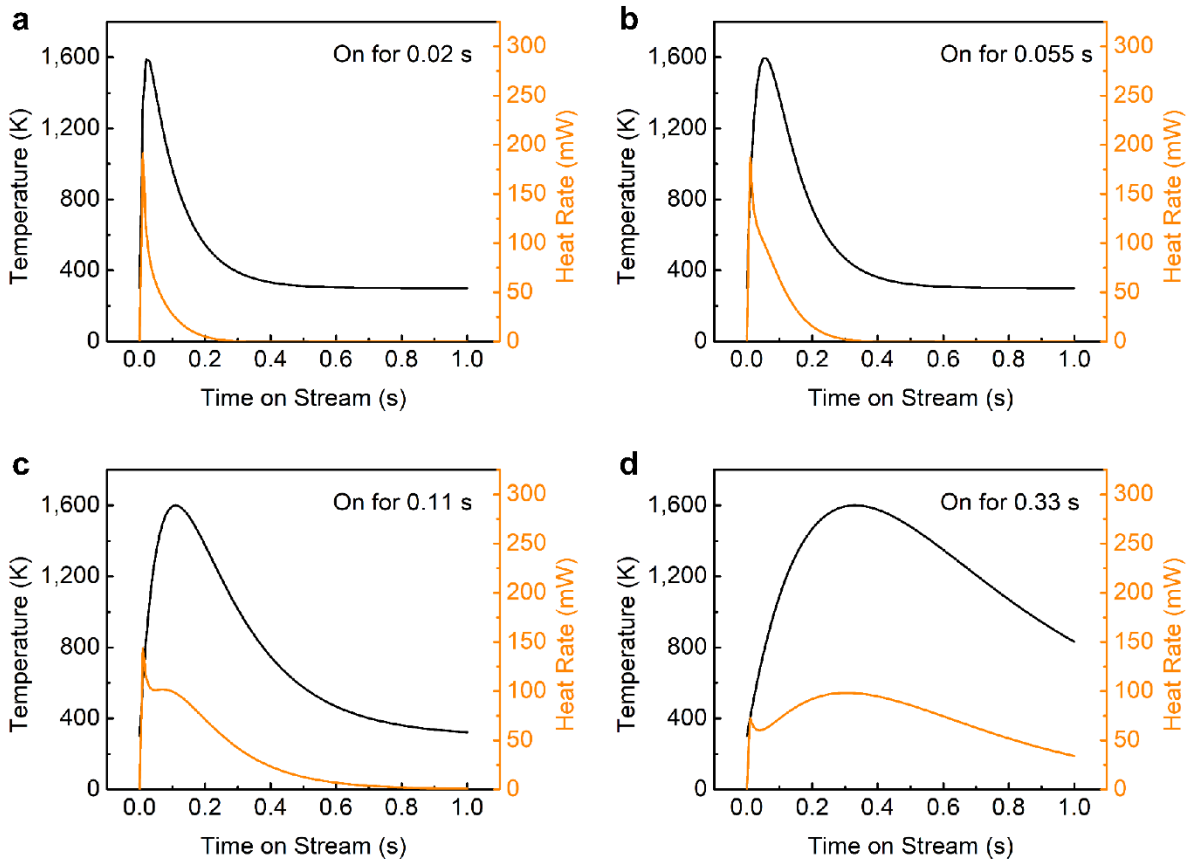

Supplementary Figure 17. Effect of pulse duration on the heat rate (energy cost) for PHQ with an inert gas (N_2), including (a) 0.02 s on, 0.98 s off; (b) 0.055 s on, 0.945 s off; (c) 0.11 s on, 0.89 s off; and (d) 0.33 s on, 0.67 s off. Theoretical temperature profiles based on the pulse function reported by Zhang and Liu[59] were used for these simulations.

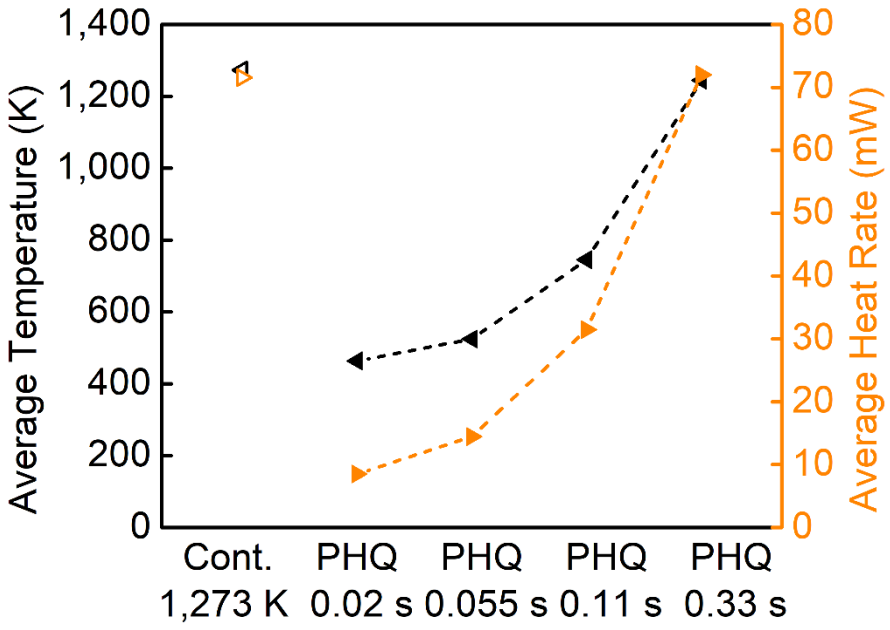

Supplementary Figure 18. The average temperature (black) and average heat rate (orange) of continuous heating (open triangles) and PHQ (solid triangles). PHQ reduces the system energy cost when the pulse duration is shorter than 0.33 s over a period of 1 s.

Supplementary Discussion 14

Our SEM results (Supplementary Figure 19) show clear difference between the Ru catalysts during PHQ and continuous heating at T_{high}. The Ru nanoparticles retained their original size and distribution after PHQ for 1 h, but are severely sintered after continuous heating at T_{high} for the same duration.

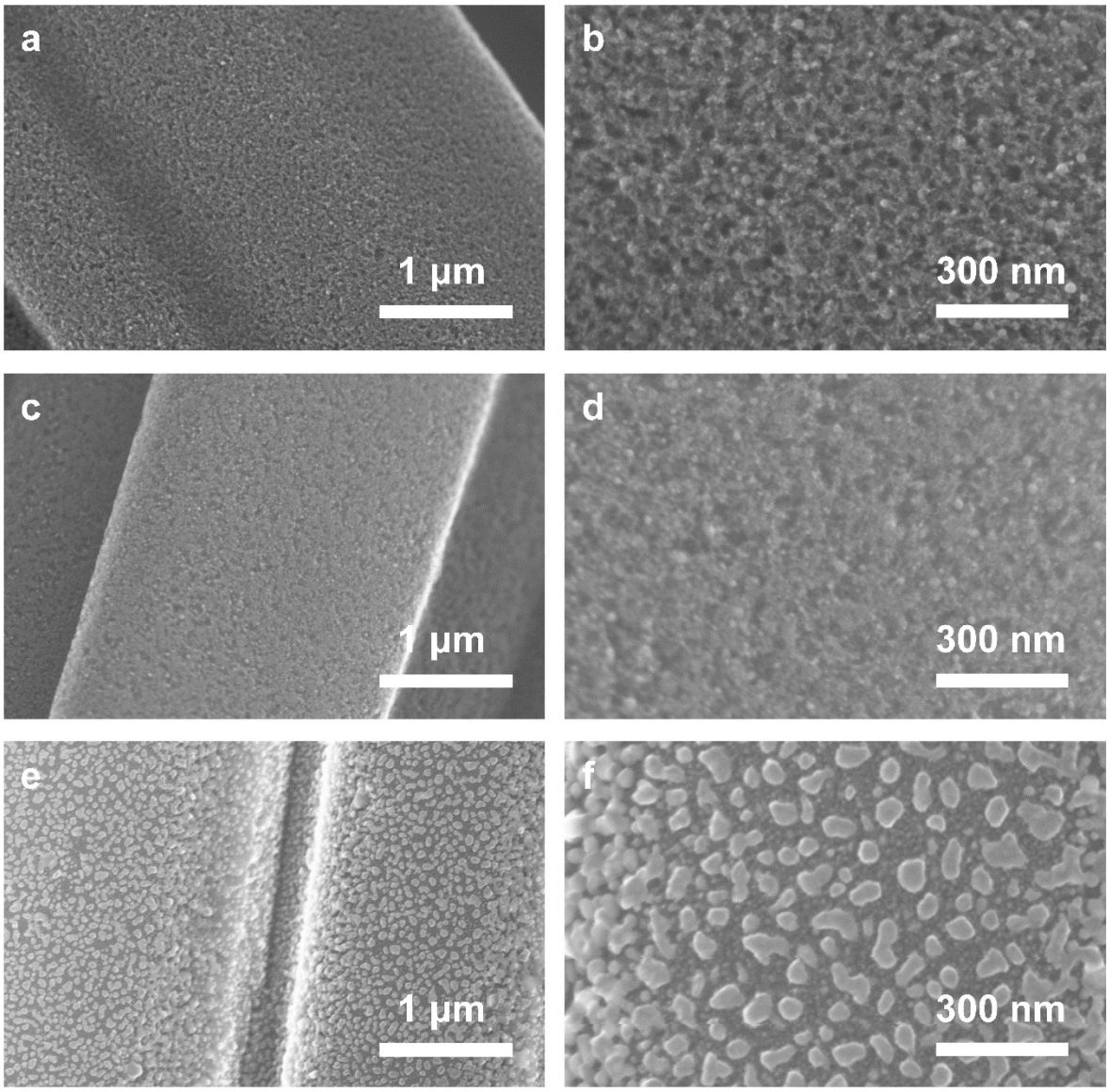

Supplementary Figure 19. SEM images showing the Ru catalyst morphological evolution during NH_3 synthesis by continuous heating (at 1,400 K, corresponding to T_{high} of PHQ) and PHQ (0.11 s on, 0.99 s off; T_{high} of 1,400 K). Pristine Ru nanoparticles loaded on carbon felt at (a) low and (b) high magnifications. Ru nanoparticles loaded on carbon felt after PHQ for 1 h at (c) low and (d) high magnifications. Ru nanoparticles loaded on carbon felt after continuous heating for 1 h at (e) low and (f) high magnifications.

Taking the morphological evolution of the catalyst into consideration, we conducted thermochemical modeling to simulated NH_3 synthesis scenarios with PHQ (0.11 s on, 0.99 s off; T_{high} of 1,400 K; $T_{avg.}$ of ~900 K) and continuous heating at a series of temperatures (1,400 K, 900 K, and 700 K), as shown in Supplementary Figure 20. PHQ exhibits much better performance compared to continuous heating at various temperatures.

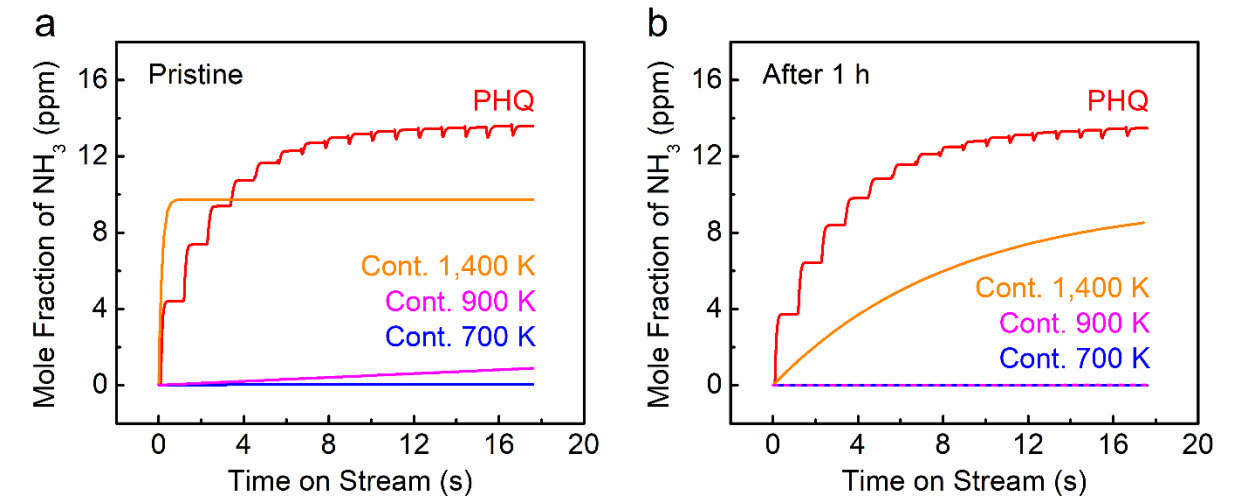

Supplementary Figure 20. Thermochemical modeling of NH_3 synthesis scenarios with PHQ (0.11 s on, 0.99 s off; T_{high} of 1,400 K; $T_{avg.}$ of ~900 K) and continuous heating at a series of temperatures (1,400 K, 900 K, and 700 K). (a) Modeling with pristine catalysts for PHQ and continuous heating. (b) Modeling with used catalysts for PHQ and continuous heating after taking into consideration the catalyst morphological evolution (Fig. 4d and 4e in the main text).

Supplementary Discussion 15

Characteristic timescales for the self-healing of carbon defects (Supplementary Figure 21) and the migration of Fe-H (Supplementary Figure 22) were both calculated using a temperature of 1,300 K based on the transition state theory. Note that T_{high} of the PHQ process was selected to ensure the robustness of the modeling results. According to Equation 18 in the Supplementary Methods section, the upper limit of the temperature used in the model leads to the shortest timescales of these undesired processes. The pulse heating duration (*e.g.*, 0.11 s) by PHQ is shorter than the lowest timescales of these undesired processes.

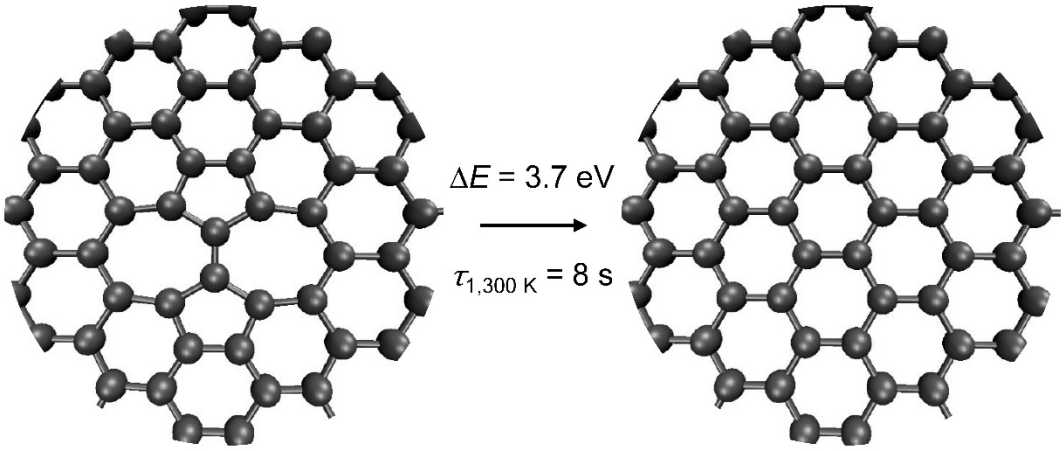

Supplementary Figure 21. Characteristic activation barrier and timescale for the self-healing of carbon defects at 1,300 K. Dark grey, carbon.

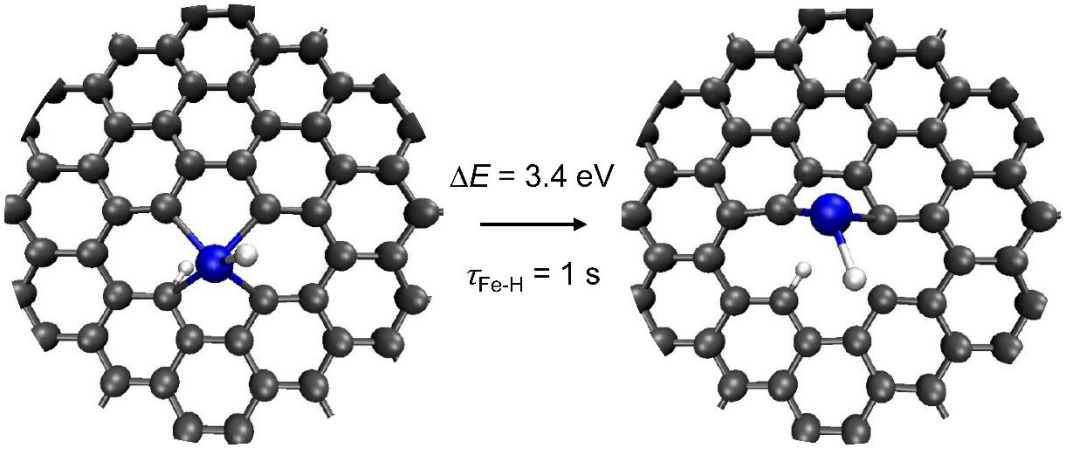

Supplementary Figure 22. Characteristic activation barrier and timescale for the migration of Fe-H at 1,300 K. Dark grey, carbon; blue, iron; white, hydrogen.

Supplementary References

42. Yao, Y. *et al.* Carbothermal shock synthesis of high-entropy-alloy nanoparticles. *Science* **359**, 1489-1494 (2018).
43. Jacob, R. J., Kline, D. J. & Zachariah, M. R. High speed 2-dimensional temperature measurements of nanothermite composites: probing thermal vs. gas generation effects. *J. Appl. Phys.* **123**, 115902 (2018).
44. Zamel, N., Li, X., Shen, J., Becker, J. & Wiegmann, A. Estimating effective thermal conductivity in carbon paper diffusion media. *Chem. Eng. Sci.* **65**, 3994-4006 (2010).
45. Teertstra, P., Karimi, G. & Li, X. Measurement of in-plane effective thermal conductivity in PEM fuel cell diffusion media. *Electrochim. Acta* **56**, 1670-1675 (2011).
46. Ozden, A., Shahgaldi, S., Li, X. & Hamdullahpur, F. A review of gas diffusion layers for proton exchange membrane fuel cells—With a focus on characteristics, characterization techniques, materials and designs. *Prog. Energ. Combust.* **74**, 50-102 (2019).
47. Burheim, O. S., Pharoah, J. G., Lampert, H., Vie, P. J. S. & Kjelstrup, S. Through-plane thermal conductivity of PEMFC porous transport layers. *J. Fuel Cell Sci. Technol.* **8**, 021013 (2011).
48. Augustin, G., Davila, S., Udiljak, T., Vedrina, D. S. & Bagatin, D. Determination of spatial distribution of increase in bone temperature during drilling by infrared thermography: preliminary report. *Arch. Orthop. Traum. Su.* **129**, 703-709 (2009).
49. Gurvich, L. V., Veyts, I. V. & Alcock, C. B. Thermodynamic properties of individual substances, 4th ed., vols. 1 and 2, *Hemisphere, New York* (1989).
50. Afshar, R., Cogley, A. C. & Saxena, S. C. Thermal conductivity of methane at atmospheric pressure in the temperature range of 360-1275 K. *J. Heat Transfer* **102**, 163-167 (1980).
51. Dawe, R. A., Maitland, G. C., Rigby, M. & Smith, E. B. High temperature viscosities and intermolecular forces of quasi-spherical molecules. *Faraday Soc.* **66**, 1955-1965 (1970).
52. Chen, S. H. P. & Saxena, S. C. Thermal conductivity of argon in the temperature range 350 to 2500 K. *Mol. Phys.* **29**, 455-466 (1975).
53. Guevara, F. A., McInteer, B. B. & Wageman, W. E. High-temperature viscosity ratios for hydrogen, helium, argon, and nitrogen. *Phys. Fluids* **12**, 2493-2505 (1969).
54. Dawe, R. A. & Smith, E. B. Viscosity of argon at high temperatures. *Science* **163**, 675-676 (1969).
55. Alkandry, H., Boyd, I. & Martin, A. Comparison of models for mixture transport properties for numerical simulations of ablative heat-shields. *51st AIAA Aerospace Sciences Meetings* **0303** (2013).
56. Mokhatab, S. & Poe, W. A. Handbook of natural gas transmission and processing. *Gulf Professional Publishing* (2012).
57. Wang, K., Villano, S. M. & Dean, A. M. Fundamentally-based kinetic model for propene pyrolysis. *Combust. Flame* **162**, 4456-4470 (2015).
58. Kee, R., Rupley, F. & Miller, J. Sandia National Laboratories Report SAND90-8003B. *Sandia National Laboratories* (1991).
59. Zhang, F. & Liu, S. A new function to represent the lightning return-stroke currents. *IEEE Trans. Electromagn. Compat.* **44**, 595-597 (2002).
60. Ebikade, E. O., Wang, Y., Samulewicz, N., Hasa, B. & Vlachos, D. Active learning-driven quantitative synthesis-structure-property relations for improving performance and revealing

active sites of nitrogen-doped carbon for the hydrogen evolution reaction. *React. Chem. Eng.* **5**, 2134-2147 (2020).
61. Jones, D. R. A Taxonomy of global optimization methods based on response surfaces. *J. Glob. Optim.* **21**, 345-383 (2001).
62. James, G., Witten, D., Hastie, T. & Tibshirani, R. An introduction to statistical learning: with applications in R. *Springer* (2013).
63. Balandat, M. *et al.* BoTorch: A framework for efficient Monte-Carlo Bayesian optimization. arXiv: 1910.06403 (2019).
64. Frazier, P. I. A tutorial on Bayesian optimization. arXiv:1807.02811 (2018).
65. Rasmussen, C. E. & Williams, C. Gaussian processes for machine learning. *MIT Press, Cambridge, MA* (2006).
66. Jones, D. R., Schonlau, M. & Welch, W. J. Efficient global optimization of expensive black-box functions. *J. Global Optim.* **13**, 455-492 (1998).
67. Marler, R. T. & Arora, J. S. Survey of multi-objective optimization methods for engineering. *Struct. Multidiscip. Optim.* **26**, 369-395 (2004).
68. Czyzżak, P. & Jaszkiewicz, A. Pareto simulated annealing—a metaheuristic technique for multiple-objective combinatorial optimization. *J. Multi-Criteria Decis. Anal.* **7**, 34-47 (1998).
69. Núñez, M., Lansford, J. L. & Vlachos, D. G. Optimization of the facet structure of transition-metal catalysts applied to the oxygen reduction reaction. *Nat. Chem.* **11**, 449-456 (2019).
70. Kresse, G. & Hafner, J. Ab initio molecular dynamics for liquid metals. *Phys. Rev. B* **47**, 558 (1993).
71. Kresse, G. & Hafner, J. Ab initio molecular-dynamics simulation of the liquid-metal–amorphous-semiconductor transition in germanium. *Phys. Rev. B* **49**, 14251 (1994).
72. Kresse, G. & Furthmüller, J. Efficient iterative schemes for ab initio total-energy calculations using a plane-wave basis set. *Phys. Rev. B* **54**, 11169 (1996).
73. Kresse, G. & Furthmüller, J. Efficiency of ab-initio total energy calculations for metals and semiconductors using a plane-wave basis set. *Comput. Mater. Sci.* **6**, 15-50 (1996).
74. Blöchl, P. E. Projector augmented-wave method. *Phys. Rev. B* **50**, 17953 (1994).
75. Kresse, G. & Joubert, D. From ultrasoft pseudopotentials to the projector augmented-wave method. *Phys. Rev. B* **59**, 1758 (1999).
76. Perdew J. P. *et al.* Atoms, molecules, solids, and surfaces: Applications of the generalized gradient approximation for exchange and correlation. *Phys. Rev. B* **46**, 6671 (1992).
77. Henkelman, G. & Jónsson, H. A dimer method for finding saddle points on high dimensional potential surfaces using only first derivatives. *J. Chem. Phys.* **111**, 7010-7022 (1999).
78. Henkelman, G. & Jónsson, H. Improved tangent estimate in the nudged elastic band method for finding minimum energy paths and saddle points. *J. Chem. Phys.* **113**, 9978-9985 (2000).
79. Salciccioli, M., Stamatakis, M., Caratzoulas, S. & Vlachos, D. G. A review of multiscale modeling of metal-catalyzed reactions: Mechanism development for complexity and emergent behavior. *Chem. Eng. Sci.* **66**, 4319-4355 (2011).
80. Su, Y.-Q. *et al.* Stability of heterogeneous single-atom catalysts: a scaling law mapping thermodynamics to kinetics. *npj Comput. Mater.* **6**, 144 (2020).
81. https://www.ansys.com/products/fluids/ansys-chemkin-pro
82. Zhao, H., Yang, X. & Ju, Y. Kinetic studies of ozone assisted low temperature oxidation of dimethyl ether in a flow reactor using molecular-beam mass spectrometry. *Combust. Flame* **173**, 187-194 (2016).

83. Zhao, H., Dana, A. G., Zhang, Z., Green, W. H. & Ju, Y. Experimental and modeling study of the mutual oxidation of N-pentane and nitrogen dioxide at low and high temperatures in a jet stirred reactor. *Energy* **165**, 727-738 (2018).
84. Zhao, H. *et al.* Studies of low temperature oxidation of n-pentane with nitric oxide addition in a jet stirred reactor. *Combust. Flame* **197**, 78-87 (2018).